TOPICAL REVIEW — A 40th Anniversary Celebration: Physics Research and Innovation at Ningbo University

Perovskite solar cells for emerging scenarios: Flexible wearables, indoor light harvesting, and semi-transparent photovoltaics

Haoyi Sun(孙昊一)[1,†], Yadi Zhang(张雅迪)[1,†], Meng Zhang(张萌)[1,†], Guangyao Wu(吴光耀)[1,†], Yuhong Xu(徐雨虹)[1], Wendong Zhu(朱文董)[1], Rong Xuan(宣容)[1], Xinlei Gan(甘新磊)[2], Xiaohui Liu(刘小辉)[1], Like Huang(黄立克)[1], Jing Zhang(张京)[1,‡], and Yuejin Zhu(诸跃进)[2]

[1] *School of Physical Sciences and Technology, Ningbo University, Ningbo* 315211, *China*
[2] *College of Science and Technology, Ningbo University, Ningbo* 315211, *China*

(Received 5 June 2026; revised manuscript received 5 October 2026; accepted manuscript online 13 October 2026)

The diversification of photovoltaic applications has exposed the structural limits of crystalline silicon, which is rigid, opaque, and poorly suited for low-light conditions. This review reframes the central question for perovskite solar cells (PSCs) from maximizing single-junction efficiency toward scenario-driven deployment. We focus on three application spaces where PSCs offer a direct mapping between material physics and performance requirements: flexible/wearable devices, indoor weak light harvesting, and semi-transparent photovoltaics. Four intrinsic properties underpin these scenarios: a high absorption coefficient enabling sub-300 nm absorbers, a soft defect-tolerant octahedral framework for mechanical strain, low-temperature solution processing compatible with polymer substrates, and a compositionally tunable bandgap for indoor LED matching. We review the recent progress of PSCs in the three scenarios and also show the effort of our group on efficient and stable PSCs. At last, we identify recurring bottlenecks: defects, interfaces, stability, and outline future directions including scenario-specific protocols, co-design strategies, and parallel advances in cost and recyclability.

Keywords: flexible photovoltaics, indoor photovoltaics, semi-transparent photovoltaics, progress and bottlenecks

PACS: 88.40.H–, 88.40.hj, 84.60.Jt

DOI: 10.1088/1674-1056/aeb361 **CSTR:** 32038.14.CPB.aeb361

1. Introduction

The sustained rise in global energy consumption, together with the demand for diversified energy supplies, has channeled considerable attention and capital toward the photovoltaic industry over the past decade as a complementary pathway to fossil-fuel-based electricity generation. Within this trajectory, silicon-based solar cells have constituted the mainstream technological direction throughout the decade, emerging as the primary choice for large-scale, ground-mounted power stations and securing remarkable commercial success. The ongoing diversification of photovoltaic applications, however, has exposed clear limitations of silicon solar cells. Their relatively narrow bandgap and intrinsic material characteristics make them inherently rigid, opaque, and poorly suited to low-light conditions. These constraints significantly restrict their adoption in an expanding array of emerging deployment scenarios. Figure 1(a) summarizes the inherent limitations of silicon solar cells across these scenarios. Developing new types of photovoltaic devices capable of meeting these scenario-specific requirements has therefore become an urgent priority.[1–4]

These limitations have driven the search for next-generation alternatives. In recent decades, a variety of emerging photovoltaic technologies — including thin-film solar cells based on Cu(In,Ga)Se_2(CIGS) and cadmium telluride (CdTe), organic solar cells, dye-sensitized solar cells (DSSCs), and quantum-dot solar cells — have been extensively explored as potential successors to silicon.[5,6] Although each of these candidates offers distinctive merits in terms of low-cost processing, mechanical flexibility, or tunable optoelectronic properties, they remain hindered by intrinsic limitations such as the scarcity of constituent elements, the complexity of fabrication procedures, and relatively modest efficiencies, which together restrict their large-scale deployment. Within this landscape, organic–inorganic metal halide perovskite solar cells (PSCs) have rapidly emerged as the most disruptive candidate, drawing unprecedented attention from both academia and industry. Since the first report in 2009 with a power conversion efficiency (PCE) of merely 3.8%, PSCs have soared to a certified PCE exceeding 27% in just over a decade — a pace unmatched by any other photovoltaic technology in history.[5,7]

With single-junction efficiency approaching the Shockley–Queisser limit, the central research question is shifting from how high PCE can ultimately go to the scenarios in which perovskites are genuinely indispensable. Lead-

[†]These authors contributed equally to this work.
[‡]Corresponding author. E-mail: zhangjing@nbu.edu.cn

© 2026 Chinese Physical Society and IOP Publishing Ltd. All rights, including for text and data mining, AI training, and similar technologies, are reserved.

CPB Online In-Press

ing photovoltaic enterprises are now establishing dedicated production lines for silicon–perovskite tandems. These tandem lines aim to contest the ground-mounted power-station market. Meanwhile, three emerging scenarios highlight perovskite's distinct advantages. The three scenarios are flexible wearables, indoor low-light devices, and semi-transparent building- or vehicle-integrated photovoltaics. Conventional silicon cannot compete in these application spaces. The intrinsic properties of perovskites translate directly into deployable products, as shown in Fig. 1(b); perovskites enable flexible and wearable devices.[8,9] Figure 1(c) illustrates their potential for indoor light harvesting. Figure 1(d) depicts the design of semi-transparent solar cells. The following paragraphs connect each of these scenarios with the specific material characteristics of perovskites that make them irreplaceable.

This review is organized as follows. Section 2 introduces the architecture of perovskite solar cells and the fundamental optoelectronic and mechanical properties that enable the three application scenarios discussed in this work. Sections 3, 4, and 5 review the front-edge research progress on flexible and wearable, indoor low-light, and semi-transparent perovskite photovoltaics, respectively, focusing in each case on the scenario-specific performance metrics, material strategies, and representative device-level demonstrations. Section 6 summarizes the recent progress on PSCs in our group at Ningbo University. Finally, it points out the common scientific bottlenecks across the three scenarios and outlines future research directions toward commercialization. We hope that this review will help redirect research attention from single-figure efficiency records toward the scenario-driven deployment of perovskite photovoltaics, where the technology offers an essentially irreplaceable role.

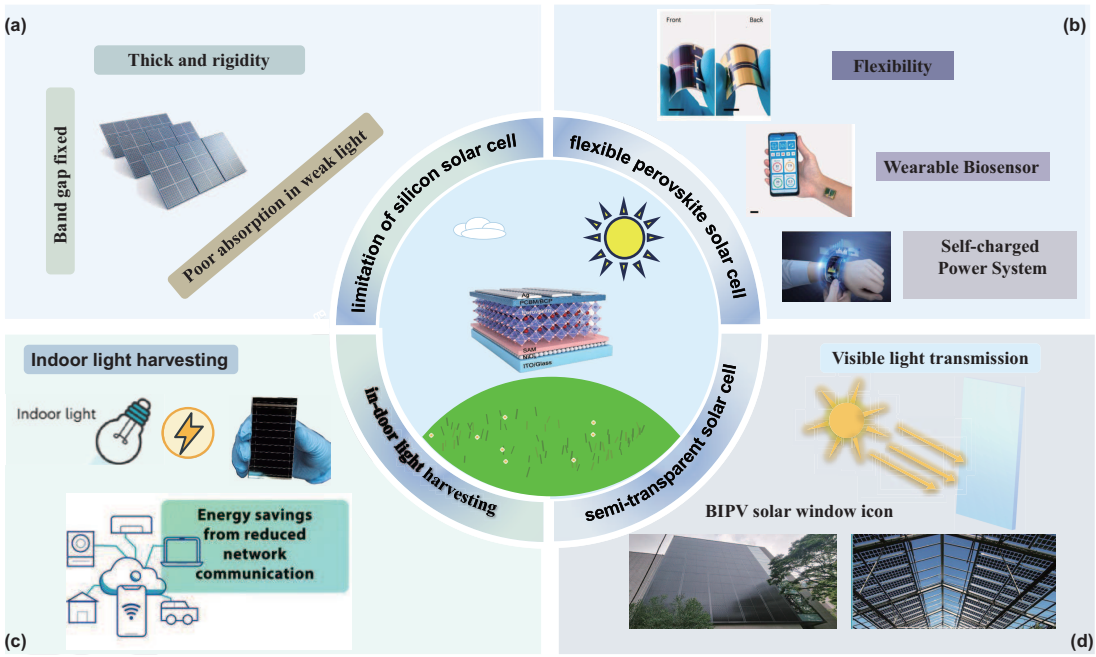


Fig. 1. (a) The limitation of silicon solar cells. (b) The advantages and applications of flexible perovskite solar cells (F-PSCs). Panel (b) is reproduced with permission from Refs. [8,9]. (c) The indoor light harvesting application. (d) The semi-transparent solar cells.

2. Fundamental characteristics of PSCs and the material properties underpinning multi-scenario applications

2.1. Structure and basic characteristics of PSCs

Early perovskite solar cells employed a mesoporous architecture that evolved directly from earlier dye-sensitized solar cells. In 2009, Kojima and co-workers first introduced $MAPbI_3$ and $MAPbBr_3$ as photosensitizers into traditional dye-sensitized cells, an effort widely regarded as the origin of perovskite solar cells as a distinct photovoltaic technology.[10,11] Subsequent work revealed that efficient charge separation, and therefore high photovoltaic performance, could be achieved by placing the perovskite in direct contact with a fullerene-based acceptor, thereby eliminating the high-temperature-sintered mesoporous TiO_2 scaffold previously considered essential.[12] Owing to its low-temperature processability, improved stability, and inherent compatibility with silicon for tandem integration, this planar design has come to dominate the field. The resulting device is a sandwich architecture in which the perovskite absorber is enclosed between dedicated electron- and hole-transport layers. Two principal configurations are now distinguished.[13] The conventional n–i–p structure places the electron-transport layer beneath the absorber, whereas the inverted p–i–n structure reverses this stack and places the hole-transport layer at

the bottom. Both planar devices dispense with the thick mesoporous scaffold and deliver high power conversion efficiencies through markedly simpler fabrication steps. Furthermore, inverted perovskite solar cells have achieved a maximum PCE of 27.5%.[7]

2.2. Intrinsic material properties underpinning the three application scenarios

The suitability of perovskites for flexible, indoor, and semi-transparent applications can be traced to their high optical absorption coefficient, their soft and highly defect-tolerant octahedral framework, their low-temperature solution processability, and their compositionally tunable bandgap, each of which maps onto one or more of the three scenarios discussed in the following sections.

Low-temperature solution processing. The solution-based processing of perovskites, and the absence of any high-temperature annealing step in inverted p–i–n device architectures, make it possible to fabricate full devices directly on plastic substrates. Charge-transport layers, perovskite absorbers, and electrodes can all be deposited below 150 °C, a thermal budget fully compatible with mainstream flexible polymer substrates such as PET and PEN. As shown in Fig. 2(a), perovskite photovoltaic layers can be fabricated via low-temperature solution-based routes.[14]

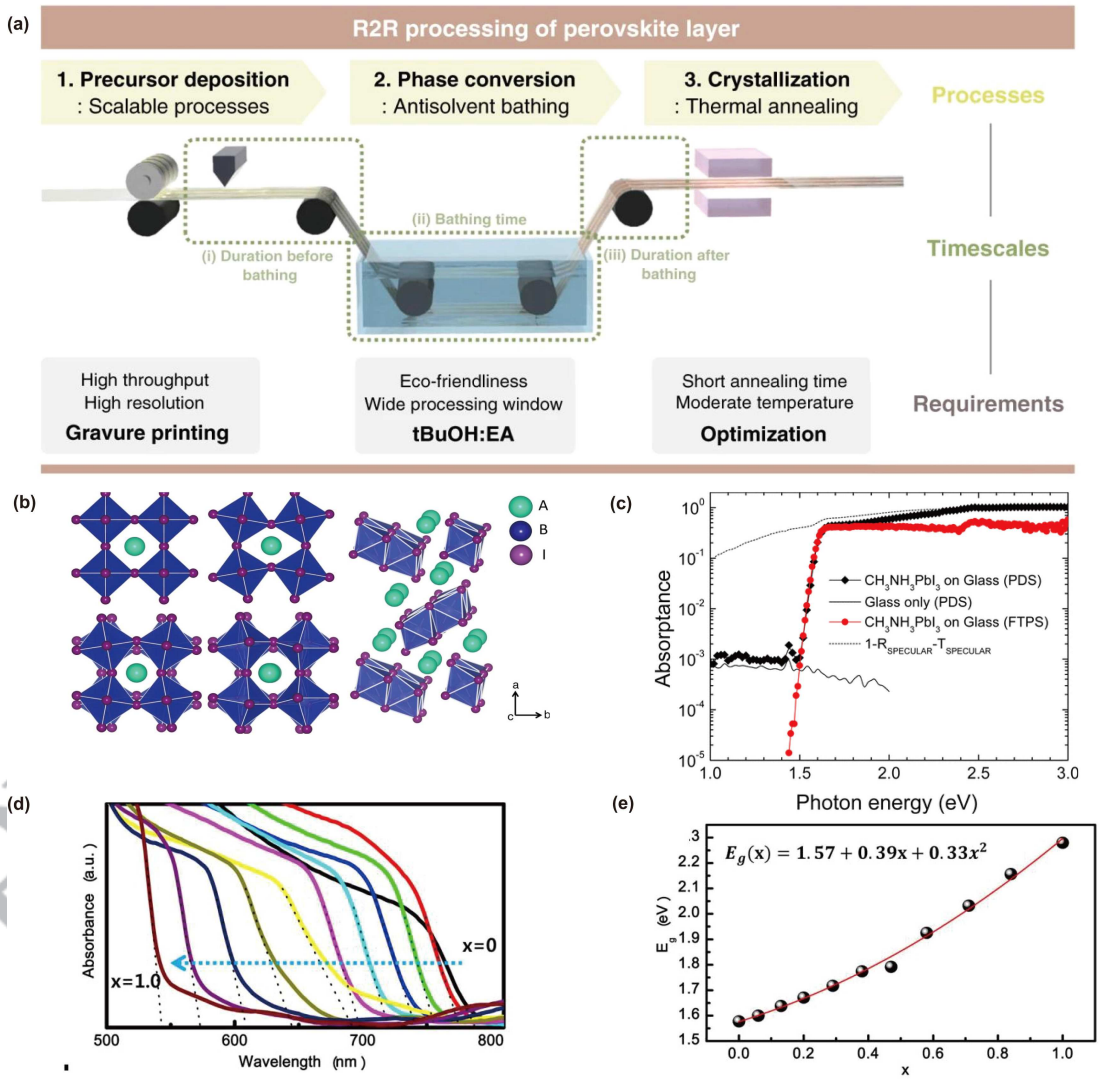


Fig. 2. (a) Schematic of the roll-to-roll (R2R) gravure-printing process for the perovskite layer. (b) Corner-sharing BX_6 octahedral framework of the ABX_3 perovskite lattice. (c) Absorptance spectra of $CH_3NH_3PbI_3$ on glass. (d) UV–vis absorption spectra of $MAPb(I_{1-x}Br_x)_3$ thin films. (e) Corresponding bandgap evolution as a function of Br composition. Panel (a) is reproduced under the terms of the CC-BY license from Ref. [14]. Panel (b) is reproduced with permission from Ref. [15]. Panel (c) is reproduced with permission from Ref. [16]. Panels (d) and (e) are reproduced with permission from Ref. [17].

Soft, defect-tolerant octahedral framework. As illustrated in Fig. 2(b), metal halide perovskites possess a corner-sharing ABX_3 framework in which the B-site metal cations are octahedrally coordinated by halide anions to form BX_6 octahedra, while the A-site cations occupy the interstitial cavities.[15] Perovskite materials exhibit a Poisson's ratio $\nu > 0.26$, which is consistent with a mechanically compliant lattice. This compliance stems from the high defect tolerance and the inherent

stretchability of the perovskite octahedral framework. The octahedra within the ABX_3 structure permit extensive modulation of the B–X–B bond angles. When the lattice is subjected to stress, these octahedra rotate much like mechanical hinges without altering the bond lengths themselves. The material can therefore accommodate significant tensile, compressive, and bending deformations without fracture.[10,11]

High optical absorption coefficient. Perovskite materials possess a remarkably high extinction coefficient of $k \approx 0.5$ at 500 nm. According to the relation $\alpha = 4\pi k/\lambda$, where α is the absorption coefficient, k is the extinction coefficient and λ is the wavelength of light, this corresponds to an absorption coefficient of approximately 1×10^5 cm^{-1} for $MAPbI_3$ at 500 nm. The steep absorption edge shown in Fig. 2(c) indicates that most incident visible photons can be harvested within only a few hundred nanometers of absorber thickness.[16] Applying the Beer–Lambert law, approximately 95% of incident photons at this wavelength are absorbed within a thickness of only 300 nm. Compared with CIGS and silicon solar cells, which require significantly thicker absorber layers, perovskite films thus achieve near-complete visible-light harvesting at a fraction of the thickness and translate this thinness directly into mechanical flexibility on polymer substrates.

Compositionally tunable bandgap. The bandgap of lead halide perovskites can be tuned through compositional engineering of the A, B, and X sites. The UV-vis absorption spectra in Fig. 2(d) further confirm this trend, showing that the absorption onset moves toward shorter wavelengths as iodide is gradually replaced by bromide. Halide substitution at the X site exerts the strongest influence. Adjusting the halide ratio modulates the relative size of the inorganic lead-halide octahedral framework and induces controlled tilting. Increasing the bromine content drives lattice contraction. As a result, the conduction band minimum shifts upward and the valence band maximum shifts downward, broadening the bandgap continuously from 1.5 eV to 2.3 eV. Figure 2(e) summarizes this composition-dependent bandgap evolution and provides the direct experimental basis for the bandgap-engineering discussion.[17] Two consequences of this bandgap tunability are directly relevant to the present review. First, indoor light sources are concentrated within the visible range (400–700 nm) and deliver intensities approximately three orders of magnitude lower than AM1.5G sunlight; under the Shockley–Queisser framework, the corresponding optimal bandgap lies near 1.9 eV.[18] Singh and co-workers demonstrated, through precise halide stoichiometry, that the perovskite bandgap can be elevated to ~ 1.8 eV, aligning the absorption edge with the emission edge of commercial white LEDs and approaching the theoretical maximum for low-light energy harvesting.[19] Second, the same tunability enables wavelength-selective absorption for semi-transparent photovoltaics: by shifting the absorption edge out of the visible range, the device preferentially absorbs ultraviolet or near-infrared photons while transmitting visible light. This optical-selectivity principle is the theoretical foundation of the semi-transparent device strategies discussed in Section 5.

Taken together, these four intrinsic properties, namely a high absorption coefficient that enables ultrathin absorbers, a soft octahedral framework that accommodates mechanical strain, a low-temperature processing window compatible with flexible substrates, and a bandgap tunable to the indoor and visible-transmission regimes, establish a direct one-to-one mapping between the material physics of perovskites and the performance requirements of the three application scenarios. The detailed material strategies, device architectures, and representative demonstrations associated with each scenario are reviewed in Sections 3, 4, and 5.

3. Flexible wearable perovskite photovoltaic devices

3.1. Basic principle and structure of F-PSCs

In recent years, flexible perovskite solar technology has matured significantly, as illustrated in Fig. 3(a), which summarizes its development trends over the past nine years.[20–26] To achieve high mechanical flexibility while being compatible with lightweight plastic substrates, F-PSCs commonly employ an inverted structure for customized design.[27,28] Traditional conventional structures require high-temperature sintering (400–500 °C) using electron transport layers such as TiO_2; exceeding the thermal tolerance limit of flexible polymer substrates induces severe thermal contraction and mechanical deformation,[29] leading to micro-cracks in the bottom transparent electrode. In contrast, all functional layers in the inverted structure can be deposited via a full solution method below 150 °C, perfectly meeting the stringent low-temperature requirements of flexible manufacturing. Additionally, conventional devices often suffer from significant hysteresis effects due to slow ion migration and inefficient electron extraction;[30] in contrast, inverted F-PSCs effectively suppress hysteresis by introducing electron transport layers such as PCBM to passivate interfaces and inhibit ion migration.[27] As illustrated in Fig. 3(b), regardless of the p–i–n or n–i–p configuration,[30] the interfacial integrity of flexible perovskite solar cells (F-PSCs) is a critical factor limiting their performance. At the buried interface, issues such as misalignment, interfacial voids, and poor contact bonding are frequently observed, which can lead to severe charge recombination. Similarly, the interface between hole transport layer (HTL)/electron transport layer (ETL) and the active layer often suffers from physical gaps (voids), hinder-

CPB Online In-Press

ing efficient extraction. Furthermore, the transparent conductive oxides (TCO) layer deposited on flexible PEN or PET substrates is highly susceptible to mechanical stress during bending, leading to crack formation. To address these mechanical and electrical losses, strategies such as utilizing non-conductive polymers/pastes or optimizing the lamination process are employed to ensure robust physical contact and mechanical durability,[30,31] as shown in Fig. 3(c).

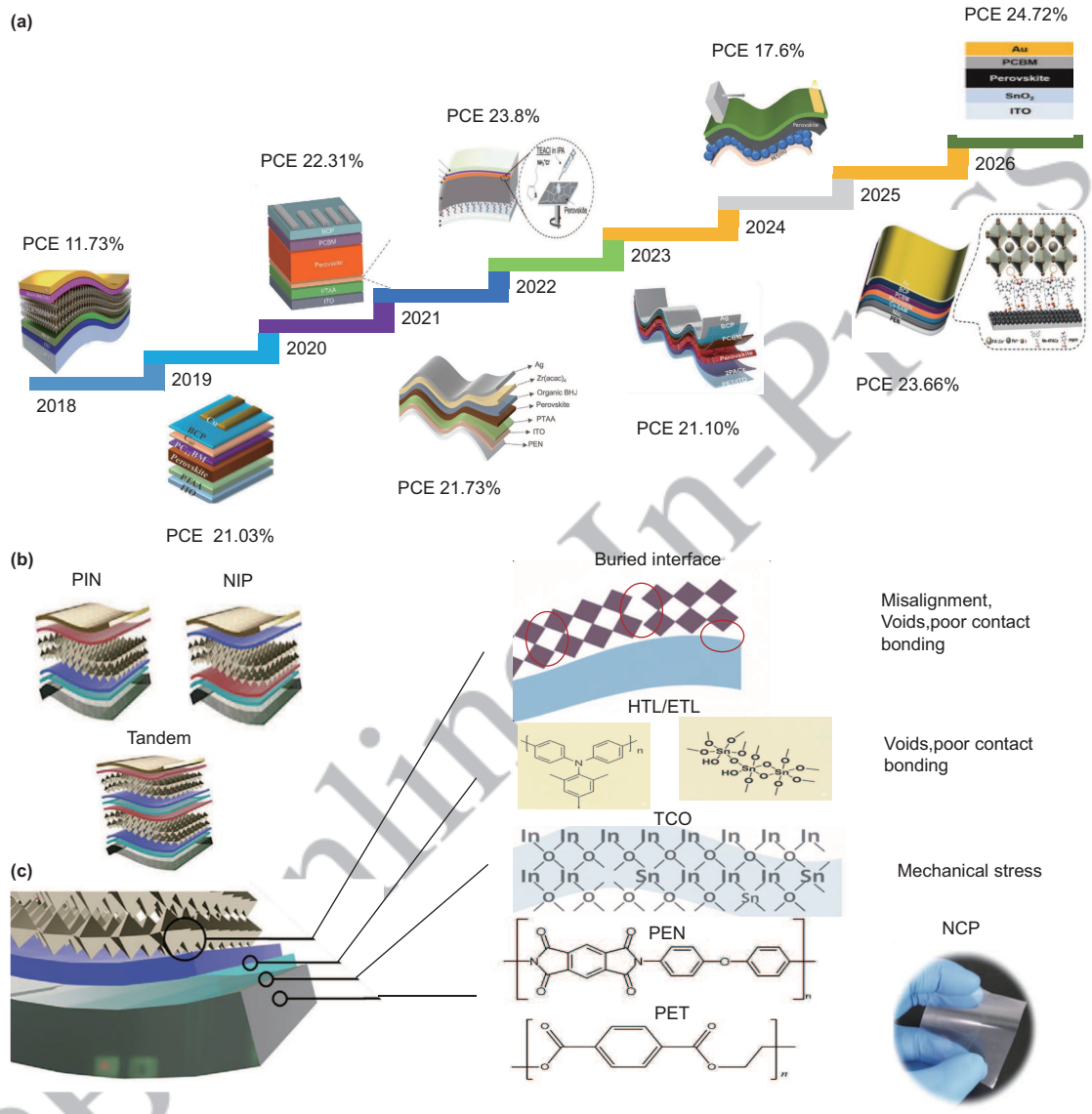


Fig. 3. Summary of efficiency evolution, architecture, and interfacial challenges in F-PSCs. (a) Efficiency evolution and structural milestones of F-PSCs from 2018 to 2026. (b) Device stacks used in F-PSC technologies, illustrating p–i–n, n–i–p, and tandem architectures from left to right. (c) Main interfacial issues that research community addresses to limit the gap between rigid and flexible substrates, including substrate/TCO contact, TCO/charge transport layer (HTL/ETL) voids, and buried interface misalignment. Panel (a) is reproduced with permission from Refs. [20–28]. Panel (b) is reproduced with permission from Ref. [30]. Panel (c) is reproduced under the terms of the CC-BY license from Ref. [32].

In the development of F-PSCs, single-junction and tandem structures exhibit distinctly different application prospects. Tandem devices significantly surpass efficiency limits by combining wide and narrow bandgaps in series; yet the increasing number of film layers and complex interconnect structures substantially amplify internal stresses during bending, readily leading to interface delamination and greatly increasing the complexity of manufacturing processes and yield control.[30–33] In contrast, single-junction devices, due to their simple structure and fewer film layers, possess exceptional bend flexibility and peel resistance, making them highly compatible with roll-to-roll (R2R) printing processes and poised to be the first to achieve commercialization in wearable and IoT applications; however, their efficiency is limited by the theoretical ceiling of a single bandgap.

F-PSCs, with their exceptional lightweight properties, high specific power, and compatibility with low-temperature solution processing, have emerged as the most promising power source for next-generation wearable electronic devices. Compared to traditional rigid devices, flexible devices must

adapt to complex human movements and meet stringent mechanical stability requirements under bending, stretching, or torsional strains.[30] Under this technological trend, the performance evaluation criteria for flexible photovoltaics have significantly expanded beyond those of rigid devices. While pursuing extremely high photoelectric conversion efficiency (PCE), comprehensive metrics such as the device's critical bending radius, performance retention after thousands of bending cycles, and specific power (W/g) crucial for portable applications — must also be considered.

3.2. Key device materials

The fabrication of F-PSCs requires systematic innovations and synergistic optimization across all functional layers. Unlike rigid devices, flexible devices must address challenges such as thermomechanical compatibility of materials and interfacial adhesion while maintaining high performance.

3.2.1. Flexible substrate

To achieve excellent flexibility and mechanical fatigue resistance while maintaining high PCE, the fabrication of F-PSCs requires systematic innovations and synergistic optimization across all functional layer materials. Current substrate types include metals, polymers, biological materials, and others, which are widely adopted due to their low cost and high flexibility. However, their low glass transition temperature limits annealing processes and often leads to poor crystallinity.[29,30] Metal foils (e.g., titanium and copper) exhibit excellent thermal stability and conductivity but must employ top-side light-transmissive or inverted structures due to their opacity. Ultra-thin flexible glass offers superior water and oxygen barrier properties as well as optical advantages, yet its inherent brittleness remains a significant challenge.[31] Additionally, to promote environmental sustainability, transparent nanocellulose paper (NCP) coated with acrylic resin has been developed as a novel flexible substrate. It not only demonstrates outstanding light transmittance and waterproof performance but can also be easily degraded through combustion, significantly mitigating the "white pollution" caused by discarded plastics.[32]

3.2.2. Electron and hole transport layers

Due to the thermal limitations of polymer substrates, the development of materials for the charge transport layer must balance low-temperature processing with flexibility. The electron transport layer primarily relies on inorganic nanocrystals such as SnO_2 and ZnO prepared via low-temperature solution methods. To enhance interface contact with flexible substrates, the incorporation of reduced graphene oxide-modified SnO_2 and other metal oxides not only significantly improves interfacial conductivity and suppresses trap-assisted recombination but also serves as a buffer layer to alleviate bending stress.[34] Low-temperature prepared SnO_2 nanocrystals often exhibit surface defects, necessitating functional molecular modification. Sun *et al.* introduced stable conformational surfactants, achieving uniform dispersion of SnO_2 nanocrystals at low temperatures, effectively suppressing electron trap recombination.[35] The hole transport layer (HTL), serving as the optoelectronic bridge of the device, typically employs organic polymers such as PTAA, where interfacial stresses are relieved through the sliding of amorphous chain segments.[36] For further optimization, Truong *et al.* designed face-to-face arranged molecular derivatives that synergistically enhance both hole extraction efficiency and mechanical compliance.[37]

3.3. Device performance optimization strategies

In the design of F-PSCs, balancing PCE with mechanical stability under stringent mechanical bending conditions and low-temperature process constraints has become a central challenge in the field. The optimization strategies to achieve this goal primarily focus on multiple dimensions, including interface regulation, crystallization kinetics, stress management, and self-healing mechanisms.

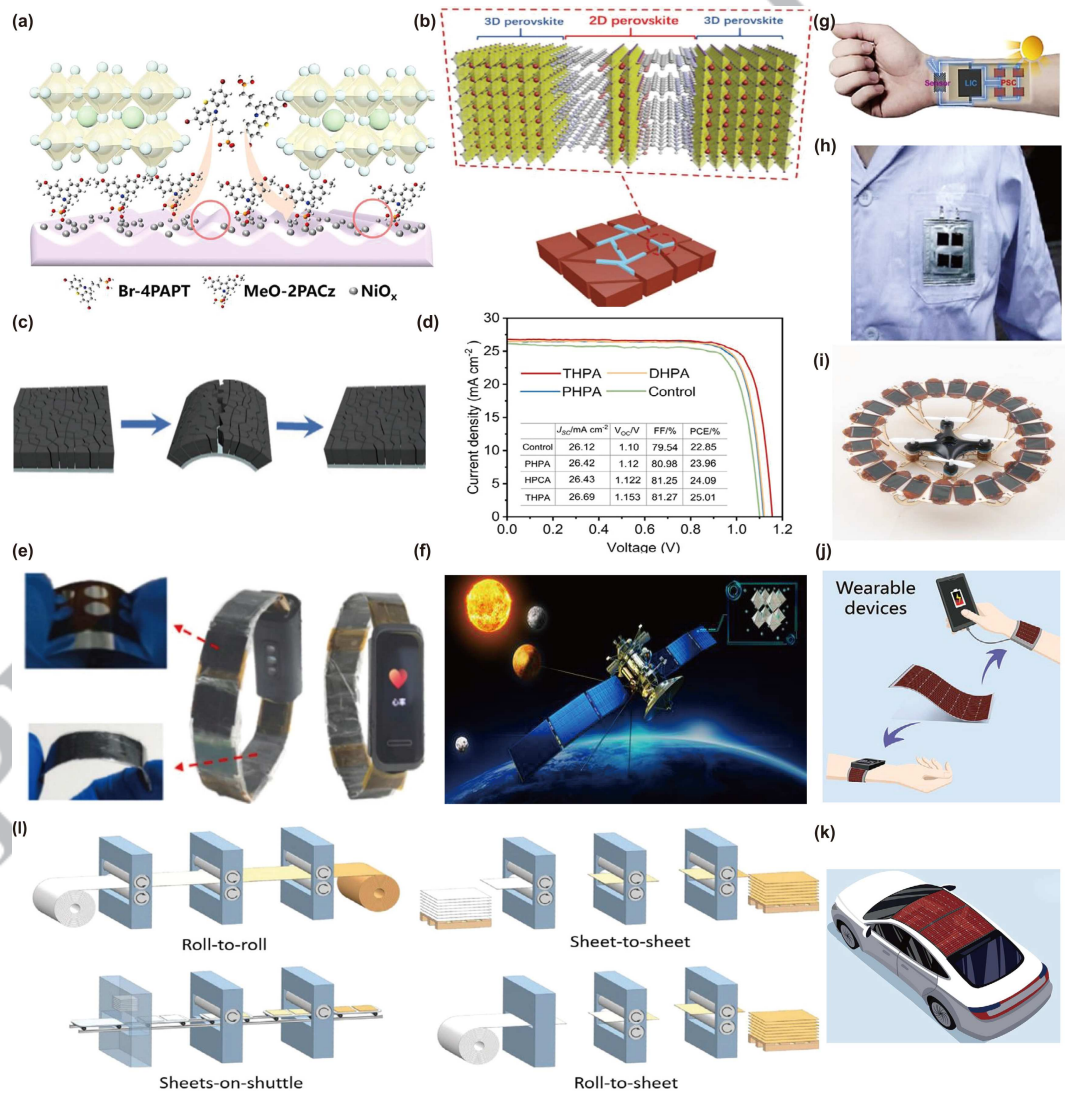
3.3.1. Interface passivation and charge transport regulation

Interface defects serve as the primary source of nonradiative recombination.[38,39] and mechanical failure in flexible perovskite solar cells, which are severely aggravated by the high surface roughness of flexible substrates. To achieve lossless carrier transport and enhance mechanical robustness, interface engineering primarily employs molecular self-assembly to construct complete, dense, and pinhole-free interfacial contacts. Han *et al.* proposed a molecular surface self-accumulation strategy that leverages the downward self-accumulation kinetics of Br-4PAPT during crystallization to enrich molecules at the substrate interface. Through this spontaneous self-assembly, these molecules form strong coordination bonds with hydroxyl or phosphate groups on the NiO_x surface, yielding an intact and compact interlayer that precisely eliminates microscopic interfacial voids, removes potential barriers in the charge extraction pathway, and suppresses crack initiation under bending, as illustrated in Fig. 4(a).[40] Meanwhile, Zhu *et al.* effectively suppressed heterointerface delamination between perovskite and the underlying electrode during bending by designing a bifacial linker, a molecular anchoring mechanism that efficiently distributes charges and significantly enhances interface stability during device operation.[41]

CPB Online In-Press

3.3.2. Crystallization dynamics and microscopic morphology engineering

Crystallization dynamics govern the morphology of perovskite films, including grain orientation, domain size, and boundary density. These features affect the photovoltaic performance and bending durability of large-area modules. To obtain compact films on flexible plastic substrates, researchers use additives to regulate intermediate phases during crystallization and control fluid flow during deposition. For example, Ma *et al.* introduced a bio-based disaccharide modifier — D-trehalose (DTA) to establish a continuous, dynamic hydrogen bond network within the perovskite films. This network not only induces lattice polarization through its polyhydroxy structure, alleviating internal micro-stresses in the material, but also provides effective spatial steric hindrance during nucleation, promoting long-range ordered grain growth. Consequently, this approach suppresses random nucleation, transforms film morphology into uniform and densely packed grains, and mitigates boundary defects, enabling the large-area module (619.9 cm^2) to achieve a steady-state efficiency of 18.86% alongside exceptional mechanical durability.[42] Complementing chemical additive engineering, fluid dynamics optimization during film deposition provides another vital route for morphology control. For instance, Li *et al.* developed an *in-situ* coating strategy for flexible all-perovskite tandem modules, which significantly improves crystal orientation uniformity and eliminates macroscopic morphological inhomogeneities on large substrates through precise control of coating fluid dynamics parameters.[43]



	J_{sc}/mA cm^{-2}	V_{oc}/V	FF/%	PCE/%
Control	26.12	1.10	79.54	22.85
PHPA	26.42	1.12	80.98	23.96
HPCA	26.43	1.122	81.25	24.09
THPA	26.69	1.153	81.27	25.01

Fig. 4. Optimization strategies, performance, and integrated applications of F-PSCs. (a) Molecular surface self-accumulation strategy of Br-4PAPT for eliminating potential barriers in the charge extraction pathway. (b) Embedded 2D/3D heterojunction strategies for developing perovskite thin films with bend resistance and high robustness. (c) Dynamic self-healing mechanism leveraging the dissociation and recombination of molecular bonds upon mechanical stress-induced cracking. (d) *J*–*V* curves demonstrating the efficiency of flexible small-area devices exceeding 25%. Demonstrations of seamless integration with electronic systems, enabling the creation of self-powered wearable microgrids. (l) Large-area modules undergoing roll-to-roll (R2R) coating processes. Panel (a) is reproduced with permission from Ref. [40]. Panel (b) is reproduced with permission from Ref. [45]. Panel (c) is reproduced with permission from Ref. [40]. Panel (d) is reproduced with permission from Ref. [45]. Panels (e)–(k) are reproduced with permission from Refs. [41,48–51]. Panel (l) is reproduced with permission from Ref. [51].

3.3.3. Mechanical flexibility and stress regulation strategies

During cyclic bending and thermal variations, flexible devices inevitably experience pronounced stress concentration, which originates from the intrinsic brittleness of perovskites and the severe thermal expansion coefficient (CTE) mismatch between the perovskite absorber and the polymer substrate. To acquire superior mechanical flexibility and fatigue resistance, stress engineering strategies predominantly incorporate functional polymers as compliant interlayers and matrices to cushion deformation strains and dissipate mechanical energy. Recent studies by Li *et al.* demonstrate that biomimetic multisite polymers not only serve as stress buffer layers but also enhance the fracture toughness of thin films via interactions between their functional groups and the perovskite lattice, maintaining effective carrier transport channels even under high deformation stresses.[44] Meanwhile, Wang *et al.* effectively mitigated the thermodynamic mismatch between the perovskite lattice and the flexible substrate caused by differences in thermal expansion coefficients by co-constructing a polyhydroxy molecular crosslinking network. This approach significantly reduced the concentration of tensile stress at the interface during bending. The combination of this molecular-level mechanical reinforcement with earlier embedded 2D/3D heterojunction strategies provides a reliable pathway for developing perovskite thin films with "bend resistance and high robustness", as illustrated in Fig. 4(b).[45]

3.3.4. Self-healing mechanism of damage

To address the fatigue-induced micro-cracks prevalent in flexible devices during their end-of-service phase, an active self-healing mechanism represents the ultimate solution for extending device lifespan. This dynamic self-healing mechanism leverages the dynamic dissociation and recombination of molecular bonds to achieve localized chemical repair upon mechanical stress-induced cracking, as illustrated in Fig. 4(c).[40] At the microscopic level, achieving autonomous self-healing fundamentally relies on introducing functional molecules that construct dynamic reversible networks along interfaces and grain boundaries.[46] Wang *et al.* fabricated embedded 2D/3D heterojunctions by introducing large-volume organic cations (such as 4-guanidinobutyric acid). The 2D perovskite phase functions as a "molecular spring" via weak van der Waals forces, effectively dissipating bending strain energy and inhibiting crack propagation through interlayer sliding, while also leveraging its wide bandgap to create an "energy funnel" effect that facilitates efficient exciton dissociation and transport into the three-dimensional bulk phase. Second, the incorporation of elastomer polymers functionalized with dynamic hydrogen-bonding or coordination groups enables the formation of an interconnected, self-healing supramolecular network along grain boundaries. When mechanical microcracks propagate under repetitive bending, the dynamic dissociation and spontaneous room-temperature re-association of these reversible bonds continuously bridge the fractured interfaces, enabling self-healing of lattice damage through dynamic dissociation and recombination of hydrogen bonds after thousands of mechanical cycles, endowing the device with exceptional mechanical robustness.[46] These strategies effectively absorb mechanical energy and suppress crack propagation. Combined with organic–inorganic alternating multilayer films for water and oxygen encapsulation,[30] the flexible device maintains high structural integrity and optoelectronic stability under severe mechanical deformation and environmental aging conditions.

3.4. Integrated applications in wearable systems

Currently, flexible photovoltaics have been successfully integrated with sensors, LEDs, and electrochemical energy storage devices. For example, Saifi *et al.* developed an ultraflexible "energy harvesting-storage system (FEHSS)" with a thickness of only 90 micrometers. By combining F-PSC modules with zinc-ion batteries and incorporating current-limiting diodes for energy management, they achieved continuous power supply to an electrocardiogram (ECG) sensor module.

For skin-worn devices, lightweight design and biocompatibility are paramount. Particularly, the toxicity of lead (Pb) in high-efficiency perovskites poses a significant threat to human safety. Studies have demonstrated that dense physical encapsulation technology effectively prevents lead leakage. In extreme tests conducted by Min *et al.*, including mechanical damage and immersion in synthetic sweat, the lead leakage from the encapsulated flexible devices was one order of magnitude lower than the drinking water safety standard set by the World Health Organization (WHO).[47]

Currently, the efficiency of flexible small-area devices has exceeded 25%, as shown in Fig. 4(d), withstanding tens of thousands of bending cycles, achieving a balance between PCE and mechanical durability.[45] The ultimate goal of F-PSCs is to achieve seamless integration with electronic systems, enabling the creation of self-powered wearable microgrids, as shown in Figs. 4(e)–4(k).[41,48–51] However, maintaining flexibility in large-area modules remains challenging: small laboratory samples (0.1 cm^2) bend easily, whereas large modules undergoing roll-to-roll (R2R), as illustrated in Fig. 4(l),[51] coating and laser marking experience laser thermal effects that damage the underlying flexible plastic substrate, leading to overall brittleness. Significant common challenges remain before full industrialization: first, preserving flexibility and efficiency during scaling of large-area mod-

CPB Online In-Press

ules; second, developing environmentally friendly encapsulation technologies with ultra-low water vapor transmission rates and high flexibility to completely eliminate lead leakage risks; third, the industry urgently needs standardized flexible mechanical testing methods and lifespan evaluation systems to standardize and accelerate commercialization.[30,52]

Revolutionary restructuring of flexible transport interfaces: Traditional brittle interfaces are being replaced by novel flexible materials. Leveraging "frictionless" interlayer sliding driven by weak van der Waals forces within two-dimensional MXenes, precise work-function control,[10,11] and microphase separation coupled with room-temperature reversible "disassociation–recombination" mechanisms in dynamic supramolecular elastomer networks,[47] the hole transport layer exhibits exceptional mechanical compliance and fracture self-healing capability, maintaining perfect ohmic contact even under extreme bending conditions.

Looking ahead, although small-area F-PSCs have achieved an excellent balance between PCE ($>25\%$) and mechanical durability.[36] However, reported bending durability is often difficult to compare directly, caused by inconsistency of bending radius, strain mode, cycle numbers and measurement conditions of each modulus. In addition, mechanical cycling is frequently evaluated separately from photovoltaic operation, whereas wearable devices may simultaneously experience illumination, electrical loading, bending, twisting, and environmental exposure during practical use. Future evaluations should therefore consistently report the bending radius or applied strain, bending frequency, total cycle number and environmental conditions. Establishing such scenario-specific mechanical testing conditions will be essential for translating laboratory flexibility records into meaningful lifetime assessments for wearable photovoltaic systems.[3,53]

4. Indoor perovskite photovoltaic devices

4.1. Application scenarios and technical requirements for indoor photovoltaics

With the explosive growth of Industry 4.0 and Internet of Things (IoT) technologies, coupled with the rapid deployment of distributed sensors indoors, the demand for indoor power supply has surged significantly. Indoor photovoltaic (IPV) cells hold the potential to power the entire IoT ecosystem, including simple devices such as humidity and temperature sensors, calculators, and wearable health monitoring devices like pulse oximeters, as well as emerging devices like indoor photocatalytic antibacterial systems — both of which require low power consumption, as shown in Fig. 5(a). Solar cells can fully meet their IPV power demands, whereas traditional disposable batteries not only incur high maintenance costs but also impose a substantial environmental burden. Therefore, indoor IPV devices can reliably provide continuous power, replacing conventional batteries. Further market projections indicate that perovskite solar cell applications in the IoT and wireless sensing sectors will grow into a multi-billion-dollar market by 2030, as shown in Fig. 5(b).[54] Consequently, the market demand for IPV has expanded markedly, making its design and application essential.[55] Common integration methods between IPV and IoT devices are shown in Fig. 5(c),[56] perovskite IPV cells can generate an average power output of 10–33 $\mu W/cm^2$ in typical office environments, sufficient to support thousands of daily wireless data transmissions for IoT devices, offering a genuine self-powered solution for distributed sensors.[57]

The evaluation criteria for indoor and outdoor photovoltaic performance differ significantly. Firstly, there is a fundamental distinction between outdoor and indoor light sources: indoor illumination constitutes only 0.1%–1% of standard sunlight (AM 1.5G, 100 mW/cm^2) (LEDs/fluorescent lamps typically range from 0.1 mW/cm^2 to 10 mW/cm^2), and indoor light sources (LEDs, fluorescent lamps) lack ultraviolet (UV) radiation, with their spectral distribution primarily concentrated in the visible light region (400–700 nm).[58] Outdoor environments, on the other hand, are characterized by broadband, high-intensity sunlight. Consequently, outdoor photovoltaics are evaluated under standard test conditions (STC: standard test conditions, AM 1.5G, 1000 W/m^2, 25°C), emphasizing long-term weather resistance and mechanical strength, whereas IPV require assessment of nonlinear responses under low irradiance conditions. However, due to the low illumination intensity indoors (typically 100–1000 lux), as shown in Fig. 5(d), and the predominantly LED/fluorescent lamp sources, which exhibit significantly narrower spectra compared to outdoor sunlight (as shown in Fig. 5(e)), optimal design of indoor energy-collecting photovoltaic devices must fully account for these differences.[59,60]

Crystalline silicon cells experience a sharp decline in fill factor (FF) under indoor low-light conditions due to current shunting losses (FF can drop below 60% when power density falls below 1 W/m^2), whereas perovskite devices maintain a high FF exceeding 75% under identical conditions, as shown in Fig. 5(f), demonstrating superior low-light performance.[61] Furthermore, the open-circuit voltage in indoor environments decreases significantly with declining light intensity, and the device's power response in low-light conditions exhibits nonlinear behavior. Therefore, the key performance indicators for indoor photovoltaic systems should include V_{OC} retention rate under low light conditions, maximum power point (MPP) efficiency, and high parallel resistance characteristics, rather than relying solely on the STC efficiency measured at outdoor user locations.

CPB Online In Press

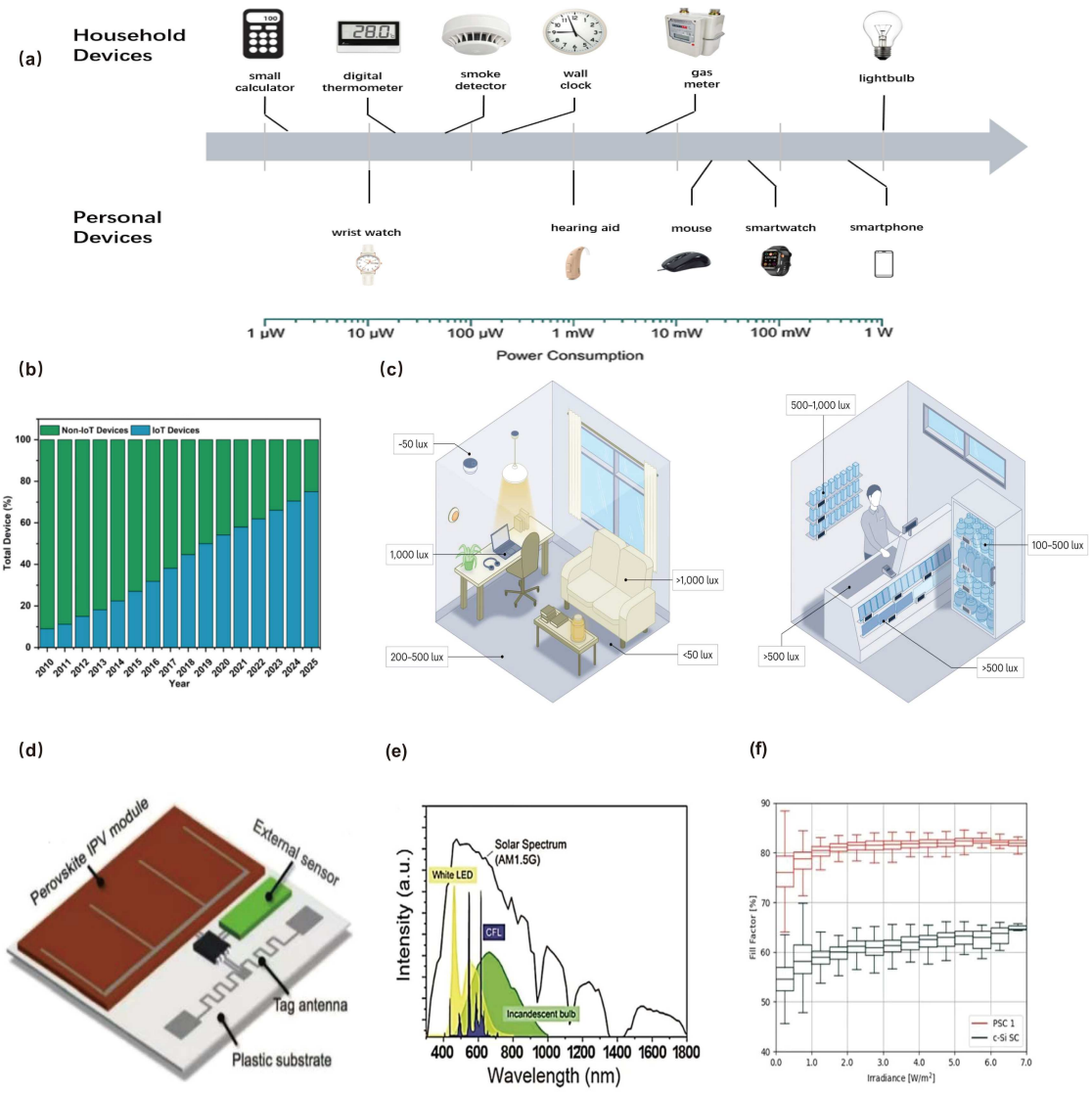


Fig. 5. (a) Common electronic devices and their power consumption. (b) Percentage growth and forecast till 2025 of IoT devices against non-IoT devices. (c) Schematic illustration of working conditions and illuminance distribution for IPV. The left panel depicts an office/home environment and the right panel a supermarket/retail environment, showing the variation in lighting intensity at different locations. Incident light levels can exceed 1000 lux near windows with direct sunlight or be as low as $\sim$ 50 lux on ceilings in corners, indicating that indoor photovoltaic materials and devices must accommodate a wide range of spatially heterogeneous illumination conditions. (d) Schematic illustration of typical perovskite solar cells interfaced with IoT devices. Panel (e) compares the spectra of white LED, fluorescent lamp (CFL), incandescent lamp, and the AM1.5G standard solar spectrum. (f) While the PSCs keep a high FF of above 75% at even below 1 W/m^2 irradiance, the FF of the c-Si SC drops below 60% compared to 78.5% under STC.(b) Reproduced with permission.[54] Copyright 2022, Statista GmbH. (c) Reproduced with permission.[56] Copyright 2025, Springer Nature. (d) Reproduced with permission.[59] Copyright 2019, Wiley-VCH GmbH. (e) Reproduced with permission.[60] Copyright 2014, IEEE. (f) Reproduced with permission.[61] Copyright 2024, American Chemical Society.

4.2. Advantages of perovskite materials under indoor light

A diverse range of materials are utilized for IPV. The high efficiency and low cost of perovskite materials have attracted considerable attention. Perovskite cells exhibit superior conversion efficiencies under indoor lighting conditions compared to other materials. Indoor light sources (e.g., LEDs, fluorescent lamps) lack ultraviolet radiation, with spectral emission primarily concentrated in the visible range (400–700 nm). Therefore, precise regulation of the perovskite bandgap becomes crucial for matching indoor spectral conditions. To this end, through the synergistic optimization of precise bandgap tuning and interfacial defect passivation, perovskite solar cells with different bandgaps can be effectively matched to the indoor light spectrum, as shown in Fig. 6(a). Moreover, due to the ABX_3 structure of perovskites, their bandgap can be easily adjusted by controlling the cation ratio at the A site and/or the halide ratio at the X site.[59,60] For perovskites, the bandgap can be tuned from 1.48 eV to 2.3 eV as the iodide content decreases. Studies show that a bandgap of 1.77 eV achieved through precise control of the iodine-to-bromine ratio (I:Br = 4:1) ensures both sufficient light absorption range (with a cutoff wavelength of 700 nm) and maximized available photon energy under indoor spectra.[62] By optimizing the bandgap, certification efficiencies exceeding 43% can be

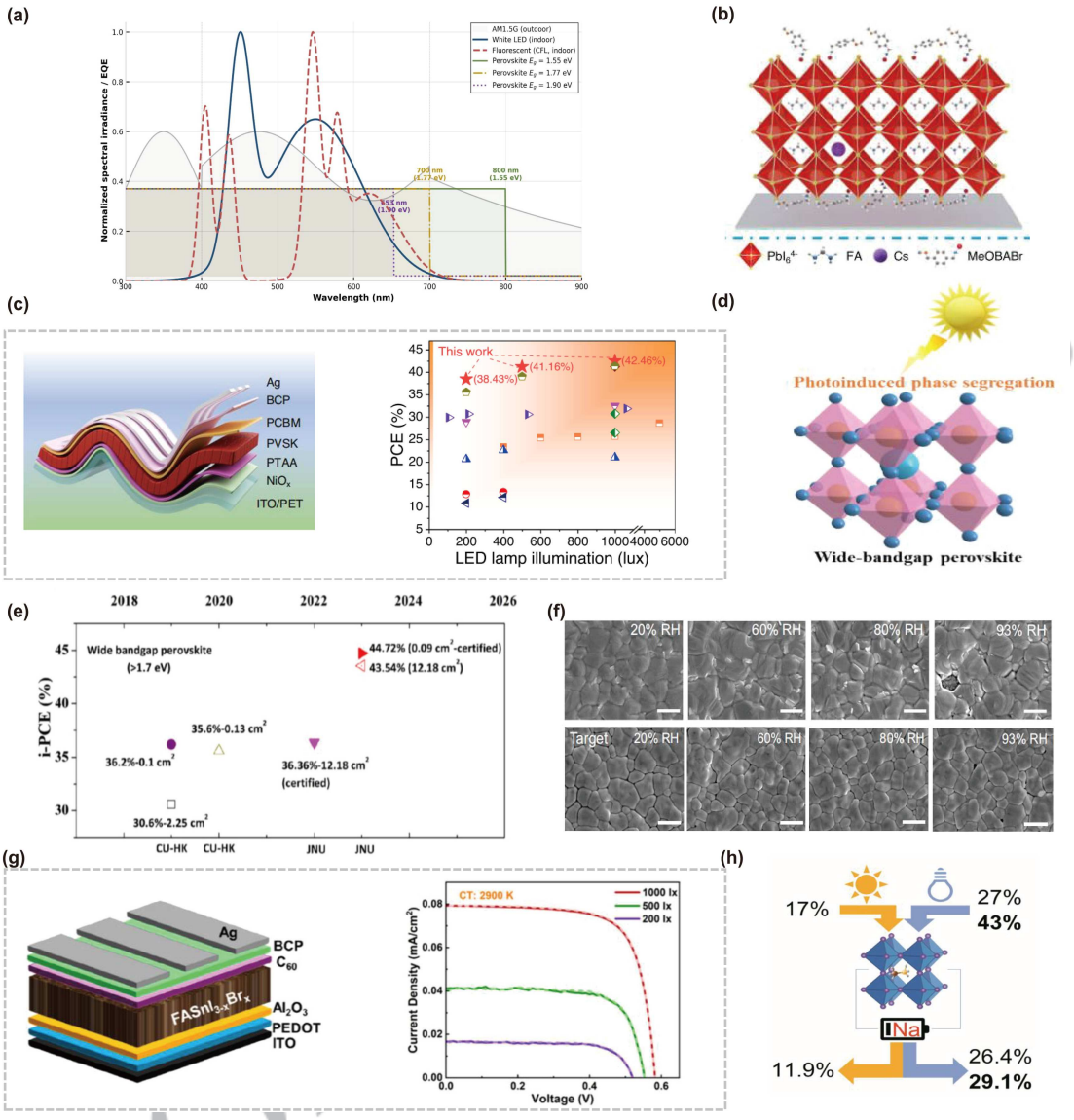


Fig. 6. (a) Normalized indoor (LED/CFL) and AM1.5G spectra overlaid with ideal perovskite EQEs, showing that the ∼ 1.90 eV bandgap better matches the LED emission (400–700 nm) than 1.55 eV $MAPbI_3$, thereby reducing thermalization losses. (b) Schematic illustration of spontaneous bifacial capping by MeOBABr on both top and bottom surfaces of the perovskite film. (c) Schematic illustration of the F-PSC structure, and its PCE under low indoor light illumination. (d) Schematic illustration of light-induced phase segregation in wide-bandgap perovskite, showing the migration of halide ions under illumination and the resulting phase-separated domains. (e) Evolution of PCEs for wide-bandgap perovskite solar cells under low indoor light illumination in recent years. (f) Comparison of perovskite films under different humidity conditions before and after optimization. (g) Schematic illustration of the lead-free perovskite structure and its photovoltaic performance under weak indoor light conditions. (h) Schematic of the $CH_3NH_3Pb(I_{0.8}Br_{0.2})_3$ perovskite mini-module directly coupled with a sodium-ion battery for indoor light harvesting and storage, showing module efficiencies of ∼ 17% (AM1.5G) and 27%–43% (LED), and overall system efficiencies of 11.9% (AM1.5G), 26.4% (500 lux LED), and 29.1% (high-intensity LED). (b)–(d) Reproduced with permission.[63] Copyright 2025, Springer Nature. (e) Reproduced with permission.[72] Copyright 2025, Elsevier. (f) Reproduced with permission.[73] Copyright 2025, American Association for the Advancement of Science (AAAS). (g) Reproduced with permission.[79] Copyright 2025, American Chemical Society. (h) Reproduced with permission.[80] Copyright 2022, Cell Press.

attained at 1000 lux. In addition to bandgap engineering, defect control and interface optimization of perovskite films are equally crucial strategies for achieving high indoor photovoltaic efficiency. Under low-light conditions, the concentration of photogenerated carriers is relatively low, rendering the impact of non-radiative recombination losses on device performance more pronounced; therefore, reducing defect density through interface passivation is of paramount importance. As shown in Fig. 6(b), Jin *et al.* introduced 4-(methoxy)benzylamine hydrobromide (MeOBABr) into the perovskite precursor solution, whereby spontaneous phase segregation led to the formation of amorphous capping layers on both the top and bottom surfaces of the perovskite film (bifacial capping).[63] These bifacial capping layers can effectively cover grain-boundary grooves and passivate surface defects, while simultaneously alleviating interfacial residual strain and promoting charge extraction. This microscopic structural optimization significantly suppresses non-radiative recombination, enabling perovskite solar cells to achieve a PCE of 42.46% under 1000 lux indoor illumination. Addi-

tionally, indoor artificial light sources exhibit significantly different Shockley–Queisser theoretical limits compared to standard sunlight. Under the AM1.5G solar spectrum, the theoretical limit efficiency for single-junction cells is approximately 33%, corresponding to an optimal bandgap of around 1.34 eV.[64] However, indoor light sources have narrow spectra concentrated primarily in the visible region (400–700 nm), with substantially reduced thermal and transmission losses, enabling a substantial improvement in the limit efficiency of single-junction devices. Wu *et al.* employed the S–Q model to systematically calculate the efficiency limits of perovskite solar cells under fluorescent lamps and white LEDs, identifying an "anomalous bandgap region" ($\approx$ 1.2–2.0 eV) in indoor lighting conditions. Within this range, the efficiency variation with bandgap differs markedly from that under solar illumination. For typical indoor lighting, the optimal bandgap is approximately 1.9 eV, significantly higher than that of conventional $CH_3NH_3PbI_3$. Ho *et al.* further demonstrated through detailed equilibrium calculations that the theoretical limit efficiency of single-junction photovoltaic devices under various indoor lighting conditions reaches 51%–57%, corresponding to an optimal bandgap range of 1.82–1.96 eV.[65] Through a combination of experiments and optical-electrical simulations, Albishi *et al.* systematically compared the performance of bandgaps of 1.55 eV, 1.72 eV, and 1.88 eV in indoor LEDs. They confirmed that the 1.72 eV bandgap exhibits optimal overall performance across various color temperatures and light intensities, while the 1.88 eV bandgap achieves a peak efficiency of 37.4% at 250 lux. The study also emphasized that reducing trap-assisted recombination is key to approaching the theoretical limit.[66]

4.3. Progress of typical device efficiency

In recent years, the efficiency of perovskite indoor photovoltaic devices has improved remarkably rapidly, making them the most efficient system among all indoor photovoltaic technologies.

The highest certified efficiency reported to date was achieved by Ma *et al.*, who employed an oil amine iodide trichloromethane solution as a dual additive to passivate bulk defects in the 1.71 eV wide-bandgap perovskite, achieving a certified efficiency of 44.72% (certified by the National Photovoltaic Industry Measurement and Testing Center (NPVM), China; measured under 1000 lux illumination from U30 fluorescent lamps, corresponding to an irradiance of 338.2 $\mu W{\cdot}cm^{-2}$) under 1000 lux illumination from U30 fluorescent lamps, with an open-circuit voltage of 1.069 V and a fill factor of 82.3%.[67] In modular applications, Ma *et al.* fabricated a 1.77 eV bandgap perovskite mini-module by precisely controlling the iodine/bromine ratio, achieving over 43% certified efficiency under 1000 lux LED illumination, demonstrating the significant potential of perovskites for large-area indoor photovoltaic applications. Zhang *et al.* developed perovskite indoor photovoltaic modules using an *in-situ* bromine vacancy defect repair strategy, achieving over 36% certified efficiency at 1000 lux illumination, providing crucial validation for the efficiency and reliability of large-area devices.[68]

Table 1. Summary of indoor photovoltaic performance of state-of-the-art IPVs.

Strategies	E_g (eV)	Illumination	Light intensity (lux)	iVoc (V)	iJsc ($\mu A{\cdot}cm^{-2}$)	iFF (%)	iPCE (%)	Certified	Refs.
OAmI:$CHCl_3$	1.71	U30 FL	1000	1.069	171.91	82.3	44.72	Yes (NPVM)	[67]
OAmI (module)	1.71	3000 K LED	1000	6.49	25.3	80	43.54	No	[62]
KI (module)	1.77	TL84 FL	1000	6.425	22.5	72.65	36.36	Yes (NPVM)	[68]
KI (cell)	1.77	3000K LED	1000	1.05	121.9	81.6	34.60	No	[68]
CMC: ICBA	1.72	4000K LED	308	3.19	49.6	63.2	27.6	No	[80]
CMC: ICBA	1.72	4000K LED (unfiltered)	$\approx$ 76 700	3.85	3370	83.4	44	No	[80]
Cl doping (triple anion)	1.65	2700 K FL	1000	1.028	123.7	78.4	36.2	No	[70]
Br substitution (Sn-based)	1.65	2900K LED	1000	0.58	80	72	11.1	No	[79]

In interface engineering, Orwat *et al.* employed peryleneimide-based sulfobetaine zwitterionic compounds as the cathode interface layer, optimizing conductivity and work function by regulating alkyl chain length, achieving an efficiency of 40.72% under a 3000 K LED (1000 lux).[69] In halide engineering, Cheng *et al.* developed the trianionic perovskite $MAPbI_{2-x}BrCl_x$, where chloride ion doping suppressed halide phase separation and reduced bulk defect density, yielding an efficiency of 36.2% under a 1000 lux fluorescent lamp while maintaining 95% of the initial efficiency after 2000 hours of continuous illumination.[70] These studies demonstrate that bandgap engineering, defect passivation, and interface optimization are effective strategies for improving the efficiency and operational stability of perovskite IPV devices under low-light conditions. Few of the indoor efficiencies listed in Table 1 are certified. Only the 44.72% cell and the 36.36% module have NPVM certification, while most other reported values come from in-house measurements. At the same illuminance of 1000 lux, irradiance ranges from 275 $\mu W{\cdot}cm^{-2}$ to 338 $\mu W{\cdot}cm^{-2}$ depending on the light source. The data also suggest that low-light performance is limited mainly by the fill factor rather than absorption. For example, the fill factor

CPB Online In-Press

of the same module drops from 83.4% to 63.2% at 300 lux. The efficiency gap of about 8 percentage points between small cells (44.72%) and mini modules (36.36%) also highlights the difficulty of scaling up devices. These results point to a need for better module performance and standardized testing, rather than a focus solely on small-cell efficiency records

4.3.1. Stability and industrialization challenges

The primary challenge in indoor applications of perovskite solar cells lies in their stability. A key issue is the phase separation phenomenon observed in wide-bandgap perovskites under light exposure, as shown in Fig. 6(d).[63] For instance, Han *et al.* proposed adding melamine as an additive to rubidium-alloyed perovskites. However, rubidium-alloyed perovskites exhibit the formation of flaky secondary phases (δ-RbpbI$_3$) during film deposition, severely compromising the lattice integrity of the film surface and creating an insulating layer that degrades both film quality and photovoltaic performance. In contrast, melamine iodide's strong coordination effect reduces the formation energy and nucleation barrier of rubidium-alloyed perovskites, enabling rubidium ions to preferentially participate in perovskite film formation over secondary phase hybrids during deposition. This approach not only eliminates surface-accumulated secondary phases but also significantly reduces defect state density and suppresses non-radiative recombination, markedly enhancing film quality. Consequently, the improved devices demonstrate substantially higher carrier diffusion coefficients and mobility.[71] Their *I*–*V* characteristics reveal enhanced shunt resistance, reduced series resistance, and lower leakage current, further confirming superior overall charge transport and reduced non-radiative recombination losses.[71] The device achieved a maximum efficiency of 25.03%, which far exceeds the PCEs previously reported in the literature within the bandgap range of 1.64–1.69 eV, and the long-term stability was also significantly improved. Thus, research on additive-based phase separation suppression has yielded numerous effective solutions. These studies have significantly boosted the efficiency of wide-bandgap perovskite solar cells under low-light conditions in recent years, as shown in Fig. 6(e).[72]

Indoor photovoltaic systems face additional challenges related to indoor humidity and thermal cycling. The relative humidity indoors typically ranges from 30% to 70%, while areas such as bathrooms and kitchens can exceed 80%. High-humidity environments are the primary cause of perovskite decomposition; suppressing the impact of humidity on perovskites can significantly improve the film quality and stability of perovskite thin films, as shown in Fig. 6(f).[73] Additionally, indoor temperature fluctuations are relatively mild, typically ranging from 15% to 35%, but frequent on/off lighting cycles are also present.[74] Regarding high indoor humidity, Wang *et al.* recommend specific encapsulation techniques that meet water vapor transmission rate (WVTR) standards below 10^{-3} g/(m^2·day), including glass-glass encapsulation, multilayer polymer/oxide stacks, and atomic layer deposition (ALD) Al_2O_3.[75] These encapsulation methods effectively suppress perovskite film degradation caused by high humidity. Moreover, ensuring proper matching of thermal expansion coefficients during device design helps mitigate accelerated ion migration due to thermal cycling.[76]

Indoor perovskite PV systems also require specialized stability testing protocols, including dedicated aging tests under indoor lighting conditions (LED/fluorescent lamps) using white LEDs (color temperature 2700–6500 K) at light intensities of 200–1000 lux at 25 °C or constant temperatures.[77] Device T80/T90 lifespans under indoor conditions must be reported, not merely under outdoor 1-hour sunlight exposure. Consequently, devices must also be tested for their long-term stability under changes in indoor humidity and temperature.

In addition, to address the toxicity bottleneck of lead-based perovskites, the development of lead-free perovskite materials is regarded as an important strategy to fundamentally resolve environmental safety concerns.[78] Among these, tin-based perovskites are considered one of the most promising alternative systems due to their photoelectric properties similar to lead-based counterparts and suitable bandgaps. However, Sn^{2+} in tin-based perovskites is highly susceptible to oxidation into Sn^{4+}, and the dimethyl sulfoxide (DMSO) solvent commonly used in traditional preparation processes significantly aggravates this oxidation, leading to severe self-p-doping and device performance degradation. Recently, Panda *et al.* proposed a tin halide perovskite $FASnI_{3-x}Br_x$ strategy based on a DMSO-free solvent system (N,N-diethylformamide/1,3-dimethyl-2-imidazolidinone, DEF:DMPU), as shown in Fig. 6(g).[79] Through halide engineering (Br^- substitution for I^-), the bandgap was tuned while simultaneously suppressing Sn^{2+} oxidation. X-ray photoelectron spectroscopy (XPS) confirmed that no Sn^{4+} signal was detected in this system, indicating that eliminating DMSO can effectively solve the oxidation problem of tin-based perovskites. Indoor photovoltaic devices fabricated based on this system achieved a PCE of 11.1% under 1000 lux illumination. Moreover, without adding any reduced agents or antioxidants, the indoor PCE of the device increased to 11.9% after storage in a nitrogen atmosphere for 6 months, demonstrating excellent intrinsic stability. Furthermore, to evaluate the performance of this DMSO-free tin-based perovskite under different indoor lighting scenarios, Panda *et al.* systematically characterized the photovoltaic output of the optimal composition $FASnI_2Br$ devices under typical LED color temperatures (warm white 2900 K) and various illumination intensities

CPB Online In-Press

(1000 lux, 500 lux, and 200 lux). As shown in Fig. 6(g), under the 2900 K light source, the device PCE gradually decreased from 11.1% at 1000 lux to 10.0% at 200 lux as the light intensity weakened.[79] These results indicate that DMSO-free tin-based perovskites can maintain a high efficiency retention rate under indoor weak-light environments and exhibit superior spectral matching with warm-white light sources, providing experimental evidence for their practical application under common indoor IoT lighting conditions. This work offers important insights for the development of high-performance, environmentally friendly lead-free perovskite materials.

In addition to the indoor photovoltaic performance of individual devices, direct coupling of perovskite modules with energy storage batteries represents an important strategy for efficient indoor light energy utilization. As shown in Fig. 6(h), Kin *et al.* constructed an indoor light harvesting–storage system based on the direct integration of a wide-bandgap $CH_3NH_3Pb(I_{0.8}Br_{0.2})_3$ perovskite mini-module and a high-rate-capable sodium-ion battery. The perovskite module achieved an efficiency of approximately 17% under AM1.5G illumination, whereas under LED lighting, the module efficiency was substantially enhanced to 27% (300 lux) and 43% (high intensity LED) owing to superior spectral matching. Furthermore, through direct coupling with the sodium-ion battery, the system attained overall efficiencies of 26.4% under dim LED light (500 lux) and 29.1% under high intensity LED, significantly surpassing its overall efficiency under solar illumination (11.9%).[80] This work provides an important paradigm for the integrated coupling of IPV and energy storage systems, demonstrating broad prospects for self-powered IoT applications.

As one of the most promising industrial applications for perovskite solar cells, IPV stands at a critical juncture transitioning from laboratory research to commercial deployment. Nevertheless, comparison of indoor photovoltaic performance across different studies remains challenging because a universally harmonized testing protocol has not yet been established. In particular, the same illuminance expressed in lux can correspond to different spectral power distributions and irradiances for LEDs with different color temperatures or for fluorescent lamps, while perovskite devices with different bandgaps respond differently to these spectra. Reported efficiencies may therefore depend strongly on the light-source spectrum, illuminance, irradiance, device area, and measurement procedure. For meaningful comparison, future studies should report the spectral power distribution and color temperature of the light source, both illuminance and irradiance, active or aperture area, stabilized power output, and T80/T90 lifetime under clearly defined indoor environmental conditions. Such harmonized reporting would enable more reliable comparison of IPV performance and facilitate the development of scenario-specific certification standards. In summary, perovskite indoor photovoltaic technology has demonstrated unparalleled efficiency advantages and application potential. However, its successful industrialization hinges on establishing standardized stability testing protocols tailored for indoor environments, overcoming challenges in thin-film quality control during large-scale production, and achieving seamless energy integration with IoT ecosystems.

5. Semi-transparent perovskite photovoltaic devices

With the acceleration of the global energy transition, photovoltaic technology is gradually developing towards the integration of energy and scenarios. In dense urban environments, traditional photovoltaic modules require a large amount of land or roof space, which limits their application in densely built areas.[81] In order to effectively utilize urban space without changing the design of buildings, semi-transparent perovskite solar cells (ST-PSCs) have been developed.

The application of ST-PSC devices is very extensive (Fig. 7(a)). Photovoltaic devices are applied to building materials or shells, such as roofs, windows or curtain walls, to generate electricity on building facades without affecting natural lighting. This is usually classified as building integrated photovoltaic (BIPV).[82] Semi-transparent BIPV structures can allow natural light to enter indoor spaces and control solar absorption without affecting indoor visibility. Of course, semi-transparent photovoltaics can also be applied to other fields. Agricultural photovoltaics is another important application direction of semi-transparent photovoltaics. By using semi-transparent photovoltaic modules with selective light transmission to cover greenhouses, some light energy can be converted into electrical energy while ensuring the photosynthetic radiation required for crop growth.[83] In addition, with the popularization of new energy vehicles and smart mobile devices, the demand for transparency of vehicle photovoltaics and mobile electronic devices is increasing. Applying ST-PSC devices to vehicle sunroofs, side windows or mobile device screens can achieve continuous power generation without changing the appearance design.[84] The development of flexible ST-PSC devices has further expanded their application prospects in wearable electronic devices.[85]

5.1. Performance evaluation of semi-transparent photovoltaic devices

Unlike traditional photovoltaic devices, ST-PSC systems require consideration not only of device performance but also of transmittance and aesthetic appearance.

CPB Online In Press

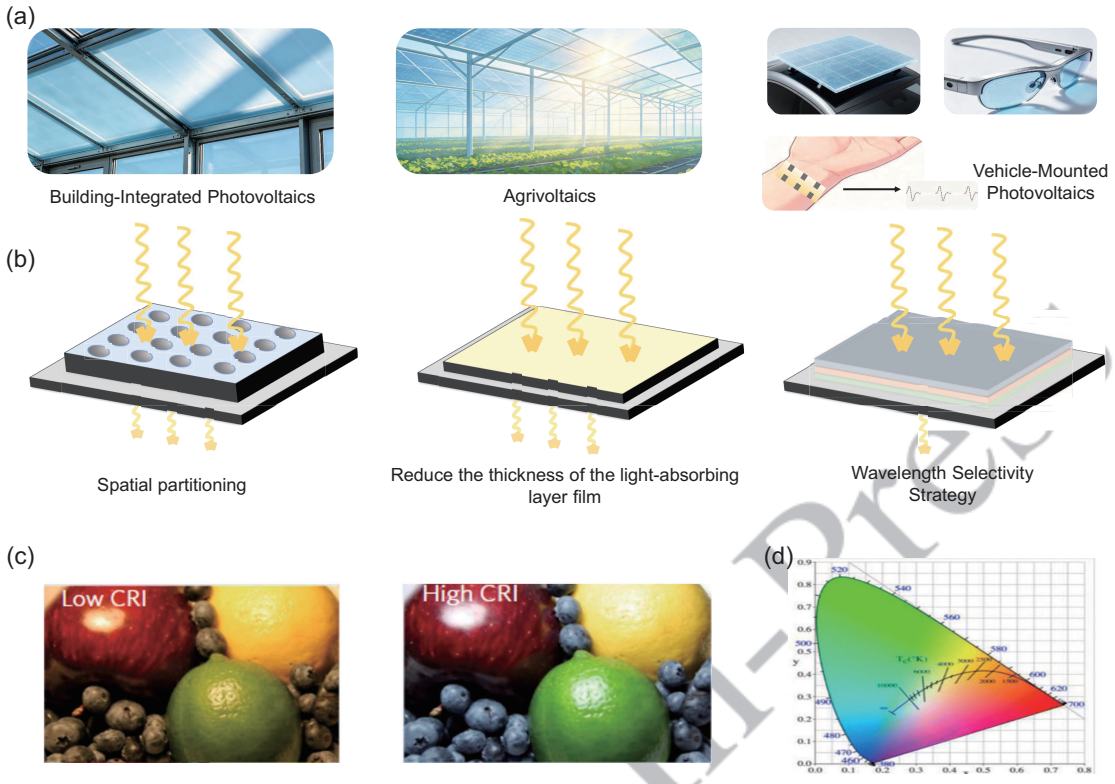


Fig. 7. (a) Schematic illustrating representative application scenarios of semi-transparent photovoltaics, including building-integrated windows, automobile glazing, electronic-device displays, and greenhouses. (b) Schematic of the different light-transmission strategies used in semi-transparent solar cells, including wavelength-selective absorption (UV/NIR-harvesting) and spatially segmented approaches. (c) Comparison between low and high color rendering indexes (CRI), illustrating how the spectral profile of the transmitted light affects the perceived color fidelity of objects viewed through the device. (d) Positions of representative semi-transparent solar cells in the CIE 1931 chromaticity diagram, with the Planckian locus indicating the chromaticity coordinates of an ideal blackbody radiator and the surrounding region defining neutral/daylight-like transmission colors. Panels (a)–(c) are reproduced with permission from Ref. [88]. Panel (d) is reproduced with permission from Ref. [88].

Average visible transmittance (AVT): AVT is a core indicator for evaluating the light transmittance of transparent photovoltaics. It is closely related to the photosensitivity of the human eye and can be expressed as[86]

$$\mathrm{AVT} = \frac{\int T(\lambda)\cdot V(\lambda)\cdot \mathrm{AM1.5G}(\lambda)\,\mathrm{d}\lambda}{\int V(\lambda)\cdot \mathrm{AM1.5G}(\lambda)\,\mathrm{d}\lambda}, \tag{1}$$

where $T(\lambda)$ is the transmittance, $V(\lambda)$ represents the human eye's response to visible light, and AM1.5G is the solar photon flux under illumination. The integration is performed over a sufficiently long wavelength range to completely cover visible light. AVT reflects the device transparency perceived by the human eye and is a quantitative standard for measuring the transparency of transparent photovoltaics. Usually, 60% AVT is used as the dividing line between TPV and ST-PSCs, because glass with an AVT value of more than 60% appears transparent, while glass with an AVT value of less than 50% begins to appear dark, colored, or reflective.[87,88]

CRI is used to evaluate the color fidelity of light passing through semi-transparent photovoltaic devices. For architectural window applications, CRI is a particularly important test indicator. If the light passing through the window has a serious color deviation, it will affect the visual comfort and working environment of the people inside. The CRI value ranges from 0 to 100, where higher values indicate that the transmitted light renders colors more accurately, and lower values indicate poorer color reproduction capability (Fig. 7(b)).[88] Generally speaking, light sources or transparent media with a CRI of at least 70 are considered to be of good quality, while those with a CRI higher than 85 are considered to be of the highest quality. CRI is calculated as follows:[89,90]

$$\mathrm{CRI} = \frac{1}{8}\sum_{i=1}^{8}\left[100 - 4.6\sqrt{(\Delta *_u^i)^2 + (\Delta *_v^i)^2 + (\Delta *_u^i)^2}\right]. \tag{2}$$

There is an inherent trade-off between AVT and PCE: increasing transmittance will inevitably reduce light absorption, thereby reducing device efficiency. In order to comprehensively evaluate the performance of transparent devices, Traverse *et al.* introduced a new performance index called light utilization efficiency (LUE),[86]

$$\mathrm{LUE} = \mathrm{PCE} \times \mathrm{AVT}. \tag{3}$$

Devices with high transmittance but low conversion efficiency, or high conversion efficiency but low transmittance, typically have low LUE. Therefore, LUE comprehensively reflects a device's performance in both power generation and light transmission, providing a clear picture of its overall performance after the trade-off between the two.

CPB Online First Preview

Color temperature assessment is mainly used to reflect the aesthetics and visual comfort of devices and to help determine whether the light is neutral.[91] Correlated color temperature (CCT) mainly characterizes the perception of the warmth or coolness of the light source. The CCT of cool colors exceeds 5000 K, while the CCT of warm colors is between 2700 K and 3000 K.[92,93] In addition, CCT is one of the most critical and widely used colorimetric measurement indicators.[94]

For the application of semi-transparent photovoltaic devices, the human eye's perception of color and transparency is crucial, as recognition is highly dependent on the spectral response of the target. To evaluate the perception of semi-transparent planar heterojunction perovskite solar cells, we can estimate it using the CIE 1931 chromaticity diagram.[95] Based on the CIE 1931 XYZ color system (see Fig. 7(c)), we calculate the tristimulus values (X, Y, Z) by measuring spectral transmittance, the spectral distribution of the D65 standard light source, and the color matching function, and then convert them into chromaticity coordinates (x, y). Commonly used incident light sources are D65 (0.3128, 0.3290) or AM 1.5G (0.3202, 0.3324), as both are close to white light (0.33, 0.33) and have good color neutrality.[88]

5.2. Semi-transparent photovoltaic technology

Semi-transparent photovoltaics (STPV) have developed rapidly and can be mainly divided into traditional thin film technology and emerging photovoltaic technology.[96] Among them, emerging photovoltaic technologies have significantly improved PCE.[97] The chemical formula of perovskite is ABX_3, where A is a small cation, B is a divalent metal cation, and X is a halide. Changing these elements in the composition of perovskite can affect its properties, such as bandgap, stability, and diffusion length.[98] PSCs possess high absorption coefficients, high carrier mobility, and long charge diffusion lengths, making them of great research value.[99] The core challenge for ST-PSCs is the contradiction between PCE and AVT. The following discussion will focus on ST-PSCs, with an emphasis on the balance between efficiency and transparency. The discussion will focus on three aspects: controlling the film thickness, adjusting the bandgap, and microstructure engineering.

5.2.1. Microstructure regulation

ST-PSCs must balance power conversion efficiency with light transmittance. Microstructure engineering addresses this challenge through spatial or optical partitioning. Instead of relying solely on a thinner perovskite layer, it assigns different regions or components of incident light to power generation and transmission. This design aims to achieve semi-transparency while maintaining efficiency. Based on this principle, researchers have developed strategies that modify the perovskite layer, electrodes, or optical polarization layer.

The first technical approach involves spatial partitioning within the perovskite layer. For example, Wang[100] regulated the perovskite crystallization process through a supramolecular dynamic coordination strategy, inducing it to grow in segments, and finally formed island nanocrystals composed of low-dimensional structures. Unlike the preparation of dense films, this strategy aims to induce the formation of discontinuous, nanoscale island perovskite crystals on the substrate. Light can pass directly through the gaps between the island structures, thereby significantly improving the AVT of the device without significantly reducing the light absorption efficiency (because the island structure can enhance light scattering and reabsorption). The essence of this method lies in partitioning the perovskite layer into regions for power generation and light-transmitting voids; however, light transmittance remains influenced to some extent by the perovskite coverage area and its absorption characteristics.

In addition to the aforementioned method of inducing the formation of island nanocrystals, the bottom electrode can also be engineered with a three-dimensional mesh or nanomesh structure; this approach transfers the compartmentalization of the perovskite layer to the electrode, further decoupling light transmittance from the intrinsic absorption characteristics of the perovskite itself. Of course, compared to standard devices, the light-transmitting areas of the grid do not contribute to power generation; consequently, the power output per unit area remains lower than that of opaque devices of the same type. The three-dimensional mesh strategy uses a conductive mesh (such as metal nanomesh) as the bottom electrode and framework, and perovskite material fills the pores of the mesh. The device will be divided into active areas (within the mesh, generating electricity) and a transparent area (between the mesh, transmitting light). The transmittance is mainly determined by the geometry of the mesh (such as pore size and line width) (Fig. 8(a)) and has little correlation with the absorption characteristics of the perovskite material itself. For example, Shao *et al.*[101] used nickel mesh as the structural framework and bottom electrode, and achieved light transmission by using a micropore array (pore size 40 μm, porosity 19.8%) as the optical control area (Fig. 8(b)). At the same time, the surface of the nickel mesh and the inner wall of the pores are used as photoelectric conversion areas to deposit the functional layer of the device. The structure separates the light-transmitting region from the photoelectric conversion region, so that AVT is no longer limited by the perovskite absorption layer, and finally achieves 4.48% PCE, 16.5% AVT and a high CRI of 98.35%. For the study of nanogrid structures, Wang *et al.*[102] used the high surface tension of MoO_3 to induce the metal film

CPB Online In Press

to form an ultrathin and highly conductive nanogrid structure, and used it as a transparent electrode. In the nanogrid, gold particles are interconnected to form a continuous conductive path, which overcomes the common discontinuity problem of ultrathin metal films. The pores in the grid allow light to pass through, avoiding the strong reflection and absorption of dense metal films. The nanogrid structure achieves both high conductivity and high light transmittance, providing a feasible solution for the development of ST-PSCs. Compared to the island nanocrystals, the grid scheme achieves a more complete physical separation between the light-transmitting and power-generating regions; consequently, light transmittance is no longer dominated by the perovskite layer but is instead determined by the geometric parameters of the grid.

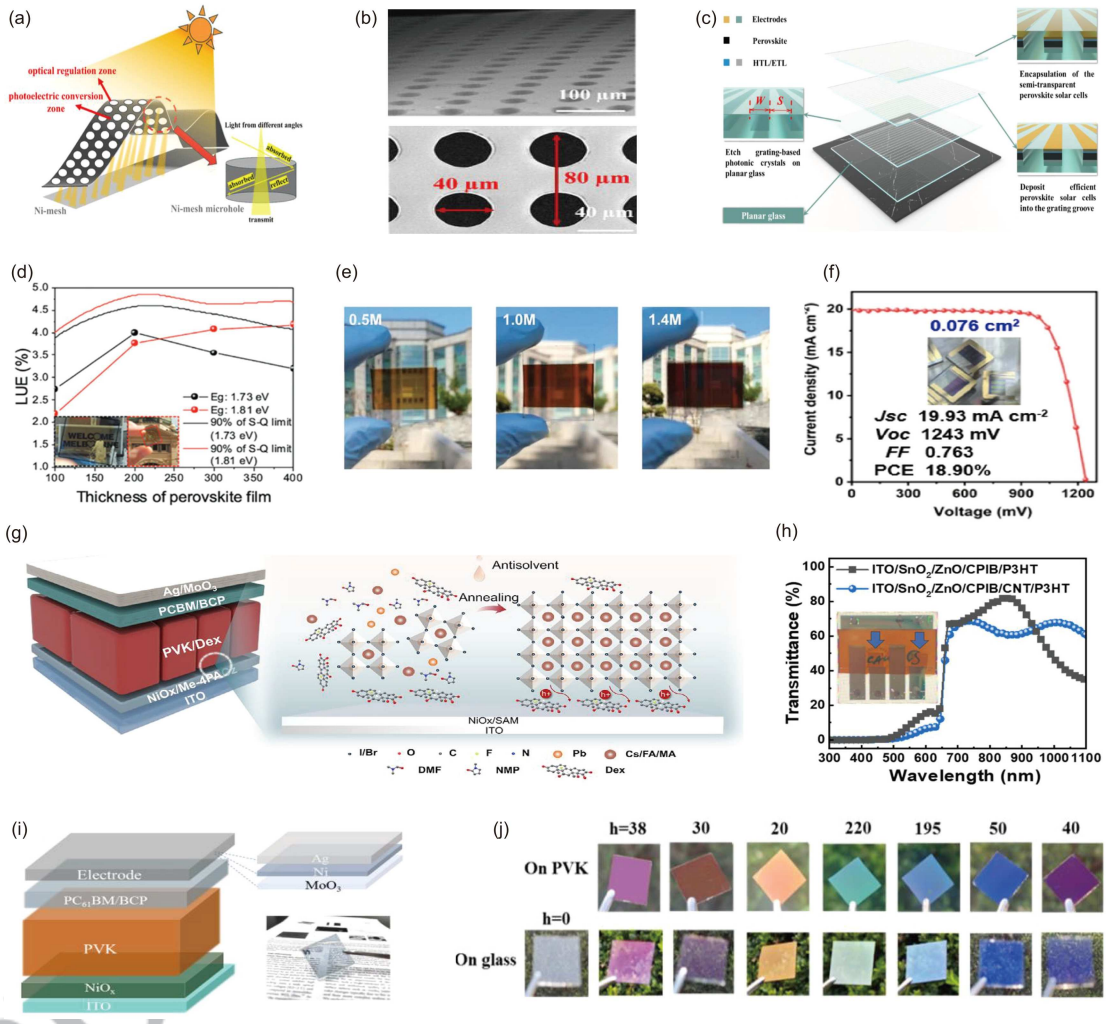


Fig. 8. (a) Schematic diagram and structural characteristics of a three-dimensional mesh structure and micro hole. (b) Nickel mesh substrate SEM including surface and local enlarged views. (c) Schematic of the semi-transparent PSC with a grating-based photonic crystal structure. (d) Dependence of LUE values on perovskite film thickness. (e) Photographs of ST-PSCs with different perovskite thicknesses prepared using different spin speeds. (f) *J*–*V* characteristics of the champion semi-transparent $CsPbI_3$ PSC with MAM buffer layer (aperture area: 0.076 cm^2). Inset: photographs of small-size semi-transparent $CsPbI_3$ PSCs. (g) Crystal structures illustrating lattice deformation. (h) Full device structure. (i) Schematic illustration of the inverted PSC with an enlarged view of the transparent top electrode. (j) PSCs and glasses with MoO_3/Ag/MoO_3 electrodes. Panels (a) and (b) are reproduced with permission from Ref. [101]. Panel (c) is reproduced with permission from Ref. [103]. Panel (d) is reproduced with permission from Ref. [105]. Panel (e) is reproduced with permission from Ref. [106]. Panel (f) is reproduced with permission from Ref. [107]. Panel (g) is reproduced with permission from Ref. [108]. Panels (h)–(j) are reproduced with permission from Ref. [120].

The third approach no longer relies on partitioning in physical area but instead achieves partitioning along the optical path by exploiting polarization selectivity. This method does not change the perovskite layer itself but etches into a grating structure on the glass substrate. By leveraging the selective absorption characteristics of photonic crystals regarding polarized light, the incident light can be modulated (Fig. 8(c)); this allows light that would otherwise be reflected or blocked by opaque electrodes to pass through, thereby achieving semi-transparency without sacrificing efficiency. For example, Zhou *et al.*[103] etched a micron-scale grating on the glass side and directly deposited a high-efficiency opaque $FAPbI_3$ solar cell in the grating trench. Utilizing a grating to exhibit different optical responses to the two orthogonal components inherently present in unpolarized sunlight: TM-polarized light (aligned parallel to the

grating) triggers a strong microcavity resonance effect, causing the light to undergo multiple reflections and absorption within the grooves — thereby enhancing absorption and reducing transmission to ensure cell efficiency. In contrast, for TE-polarized light (aligned perpendicular to the grating), the electric field is perpendicular to the grating's periodicity; this results in weak coupling with the grating structure and fails to excite strong microcavity resonance, significantly reducing light localization and the absorption path within the perovskite layer. Consequently, the majority of visible light is efficiently transmitted through the semi-transparent cell, maintaining a flat transmission spectrum and resulting in white transmitted light. Based on the high-efficiency opaque cell, the balance between PCE and AVT is achieved through optical model optimization. Compared to the first two approaches, the grating-based scheme shifts the division between power-generating and light-transmitting regions from physical space to the optical dimension; it relies less on the perovskite material itself and allows for a more refined and controllable trade-off between efficiency and transparency.

5.2.2. Thickness control of the perovskite layer

The most direct way to achieve ST-PSCs is to reduce the thickness of the perovskite light-absorbing layer. When the thickness of the perovskite layer is reduced to below 300 nm, the film can be semi-transparent.[104] Yu *et al.*[105] investigated the effects of perovskite composition on the combination of Cs, FA, MA, I, and Br. They fabricated perovskites with bandgaps of 1.73 eV and 1.82 eV and reported improved efficiency and stability of ST-PSCs (Fig. 8(d)). ST-PSCs with thicknesses ranging from 100 nm to 400 nm achieved PCE values of 4.2% to 15.4% and AVT values between 52.4% and 20.8%. Images of ST-PSCs of different thicknesses are shown in Fig. 8(e). Reducing the thickness of the perovskite layer will worsen its surface coverage and generate a large number of pinholes. Excessive thinning will also introduce lattice strain. To solve these problems, scientists have conducted the following studies.[106]

Interface buffer layer optimization: The pinholes are covered by a dense buffer layer deposited on the perovskite layer, and the device is protected from subsequent process damage. For example, Zhang *et al.*[107] formed a MAM sandwich structure buffer layer by embedding an ultrathin silver layer (about 1 nm) between two layers of molybdenum oxide (MoO_x). The key to this structure is that silver reacts *in-situ* with molybdenum oxide at the interface to generate Ag_2MoO_4, which can not only resist the plasma bombardment generated during magnetron sputtering deposition of transparent electrode (IZO) and protect the lower perovskite and hole transport layer, but also significantly improve the carrier transport and collection efficiency due to its high light transmittance and energy level matching. As shown in Fig. 8(f), the pure MoO_x blocking layer could effectively shield the perovskite layer from ITO sputter-induced damage. For the MAM structure, Ag ions are mainly distributed in the middle between the two MoO_x layers, further confirming its $MoO_x/Ag_2MoO_4/MoO_x$ sandwich configuration. Since thinning the perovskite will lead to poor coverage of the perovskite on the hole transport layer, resulting in increased interface defects and severe heat accumulation, Wang *et al.*[108] proposed a pharmacophore-guided molecular design strategy, using dexamethasone (Dex) as the interface ligand. Dex achieves multi-point synergistic anchoring at the buried interface of the perovskite/hole transport Fig. 8(g), while achieving defect passivation, band modulation and reduction of interface thermal resistance. Finally, the optimized device with an absorption layer of about 150 nm thick achieved a PCE of 15.26% under the condition of an average AVT of 20.88%, corresponding to a LUE of about 3.19%.

Crystallization regulation: During the thinning process, excessively thin films not only have difficulty forming a dense capping layer but also introduce lattice strain due to interface constraints. To address this issue, researchers have developed various strategies aimed at improving crystal quality and relieving stress. For example, Ghosh[109] used an *in-situ* strain control strategy, adding different amounts of formamidinium hydrochloride (FACl) to the $MAPbI_3$ precursor solution. The addition of FACl increased the grain size, improved crystallinity, and transformed the intrinsic compressive strain of the film into tensile strain, eliminating inhomogeneities within the film. This paper demonstrates the key role of compressive strain in stabilizing lattice rigidity and suppressing photoinduced ion migration.

5.2.3. Bandgap control

Band engineering is the core strategy for ST-PSCs to achieve spectrally selective absorption. By adjusting the halogen composition of perovskite, the absorption edge can be tuned to outside the visible light range, so that the device mainly absorbs ultraviolet and near-infrared light, while allowing visible light to pass through.[110] Transparency is mainly adjusted by adjusting the halide composition of the X site. The higher the Br content, the wider the bandgap, the enhanced absorption of short-wavelength light and the increased transmission of long-wavelength light (the sensitive area of the human eye).[106] Jin Choi's team.[111] systematically studied the $(FA_{0.85}Cs_{0.15})Pb(I_{1-x}Br_x)_3$ system, where $x = 0$, 1, and 2 correspond to bandgaps of 1.56 eV, 1.75 eV, and 1.95 eV, respectively. They found that the optimal light utilization efficiency (LUE) balance was achieved at a thickness of 65 nm for a wide bandgap perovskite with a bandgap of 1.75 eV.

CPB Online In-Press

Wide bandgap perovskites usually refer to perovskite materials with a bandgap greater than 1.65 eV.[112] Although bromine-rich perovskites are beneficial for light transmission, they face severe halide phase separation, ion migration and open-circuit voltage loss.[113] Therefore, scientists are shifting their research focus from traditional halogen component regulation to the development of multifunctional molecular passivation, dipole molecular interface modification and bromine-free direction transformation. Chen *et al.*[114] introduced sodium formate (NaFo) to modify the buried interface between the electron transport layer SnO_2 and the perovskite to address the photostability problem of wide bandgap perovskites, which suppressed the photoinduced halide phase separation of the bromine-rich system and improved the efficiency and photostability of wide bandgap perovskites. To effectively control the crystallization process, Jin *et al.*[115] introduced a bifunctional dipole molecular additive, 3,5-difluorobenzamidine hydrochloride (DFBA). DFBA forms multi-point synergistic passivation with perovskite through the coordination bond between F^- and Pb^{2+} and the hydrogen bond of NH$\cdots$I/Br. By simultaneously passivating defects and optimizing energy levels through molecular dipole engineering, battery efficiency and light transmittance can be balanced. Yoon *et al.*[116] proposed a bandgap adjustment strategy that does not depend on halogen composition. Instead of increasing the bromine content, they introduced dimethylamine (DMA) at the A site to partially replace formamidinium (FA) and used lattice expansion to widen the bandgap. This method provides a new idea for wide bandgap control.

5.3. Transparent electrode

The transparent electrode occupies a uniquely constrained position within the device stack, because it is required to transmit incident photons and to collect and laterally conduct the photogenerated carriers at the same physical interface. These two functions are not independently adjustable. Both are governed by the free-carrier concentration and the thickness of the film. Increasing either lowers the sheet resistance, yet a higher free-carrier concentration intensifies free-carrier absorption in the near-infrared following the Drude model, while a greater thickness attenuates transmittance directly through the Beer–Lambert relation. The top transparent electrode must balance the requirements of high conductivity, high transmittance, appropriate work function, and compatibility with the underlying material. Therefore, the material selection and structural design have a decisive impact on the device's efficiency, transparency, color rendering, cost, and stability.[117] Common TCOs such as indium tin oxide (ITO) have excellent optoelectronic properties, but they can damage the sensitive perovskite layer and reduce device performance when deposited.[118] The Henk J. Bolink team[119] used a full vacuum deposition process to prepare ST-PSCs. By optimizing the thickness of the perovskite layer (about 100 nm) and the back electrode ITO structure, they achieved a highly efficient and transparent top electrode without introducing an additional buffer layer. The paper proposes an interface reactive sputtering strategy, introducing polyethyleneimine (PEI) as a reactive interface layer between the C_{60} electron transport layer and ITO. PEI reacts with sputtered ITO nanoparticles to form coordination compounds, which mitigate the impact of high-energy particles, protect the integrity of the underlying C_{60} and perovskite layers, and promote carrier transport at the C_{60}/PEI/ITO interface. In addition to introducing a buffer layer, scientists have also found alternative electrode materials, such as: (1) dielectric/metal/dielectric (DMD) multilayer electrodes; (2) carbon nanotube (CNT) electrodes; and (3) conductive polymers and emerging materials.

The DMD structure adopts a sandwich configuration of transparent dielectric layer/ultrathin metal layer/transparent dielectric layer. Through the optical interference effect, the ultrathin metal layer (usually Ag, Au or Cu) can achieve high conductivity, while the dielectric layer (such as MoO_3, WO_3, ZnO) plays the role of anti-reflection and metal protection. By adjusting the thickness of each layer, the transmission spectrum and color can be effectively controlled.[117] Carbon nanotubes (CNTs) have excellent conductivity, high light transmittance, good flexibility and chemical stability. Moreover, the preparation process does not require harsh conditions such as high temperature or sputtering, which can completely avoid the use of metal electrodes, thereby reducing manufacturing costs and eliminating device instability caused by metal diffusion. Based on these advantages, Yoon *et al.*[120] first introduced CNTs synthesized by floating catalyst into all-inorganic PSC as top electrodes, as shown in Fig. 8(h). They combined hydrophobic CNTs with polymer hole transport materials to form a nano-hybrid film, which has both efficient charge collection and moisture protection functions. The conductive polymer has solution processability, good flexibility and light transmittance, and can achieve low-cost and large-area preparation. In addition, emerging materials such as metal nanowires and graphene have also shown potential in ST-PSCs top electrodes.

To address the issues of island-like growth, poor conductivity, energy level mismatch, low back-side efficiency, and monotonous appearance associated with ultrathin Ag transparent electrodes in p–i–n bifacial PSC, our team designed and fabricated a MoO_3/Ni/Ag/MoO_3 (DMD) transparent top electrode (Fig. 8(i)). MoO_3 enhances the wettability of Ag, and the 1 nm Ni seed layer modulates the electrode work function from 4.62 eV to 4.31 eV, eliminating the Schottky barrier

CPB Online In Press

between MoO_3 and Ag and forming an ohmic contact, significantly improving charge extraction efficiency. Simultaneously, Ni improves the continuity and flatness of the Ag film. Ultimately, the front-side efficiency reaches 20.8%, approaching the 22.1% of a 100 nm Ag reference device. Building upon this, as shown in Fig. 8(g), color modulation of reflected light is achieved by varying the thickness of the top MoO_3 layer (20–220 nm), while simultaneously increasing the back-side transmittance at 20–50 nm, raising the back-side efficiency from 11.95% to a maximum of 14.56%, achieving a bifacial factor of 57.6%–74.4%, and a bifacial equivalent efficiency of 24.95%. The top MoO_3 layer also provides protection, significantly improving the device's storage stability. This work offers a low-cost, easily evaporable transparent electrode solution for efficient, aesthetically pleasing, and stable bifacial PSC.[121]

Despite significant progress in efficiency, transmittance, and stability, ST-PSCs still face multiple challenges in transitioning from laboratory applications to practical use. First, there is the challenge of balancing PCE and AVT. Due to the physical repulsion between light absorption and visible light transmission in the active layer, increasing transparency can lead to insufficient photon capture and decreased photocurrent, and high transmittance is often accompanied by significant color shift. Second, large-area fabrication is constrained by process techniques; ultrathin perovskite films are prone to pinholes and discontinuities, and the large-scale, reproducible deposition of transparent electrodes (especially the top electrode) also faces bottlenecks. Third, long-term stability depends on the development of high-transmittance, high-barrier encapsulation materials, and the performance degradation of devices under complex environments such as high temperature, humidity, and ultraviolet irradiation urgently needs to be addressed. Finally, color control to meet the aesthetic requirements of BIPV remains challenging. Although methods exist to achieve full-spectrum color coverage, such optical control often comes at the cost of sacrificing some light absorption. Achieving precise color control without significantly reducing efficiency remains a key area requiring further exploration.

6. Recent progress of our group in PSCs

6.1. Efficiency promotion strategies in our group

Our group has achieved the development of high-efficiency perovskite solar cells through the implementation of several technical strategies, including nucleation-induced grain growth, energy level regulation, and defect passivation. In the context of heteronuclear-induced crystallization, we introduced zinc ions as heteronuclear to inductively grow high-quality inorganic perovskite thin films with grain sizes exceeding 5 μm, which significantly reduced grain boundary density and suppressed non-radiative recombination (Fig. 9(a)).[122] Furthermore, we constructed heteronuclear at the buried interface, achieving dual functionalities of induced crystallization and interfacial defect passivation (Fig. 9(b)).[123,124]

In terms of energy level regulation in perovskites, our team employed an aliovalent ion doping strategy to effectively modulate the built-in electric field of the devices, thereby enhancing charge carrier separation efficiency. Specifically, aliovalent Sb^{3+} doping on Pb sites in $MAPbI_3$ enabled n-type doping and elevated the Fermi level at the perovskite/electron transport layer interface, leading to an enhanced built-in electric field.[125] By incorporating the smallest metal ion Li^+, we achieved dynamic modulation of the n/p-type doping of perovskites via mobile ions.[126] The application of graphene quantum dots bearing electronegative chlorine atoms to the interface of $FA_{0.6}MA_{0.4}Sn_{0.6}Pb_{0.4}I_3$ narrow-bandgap perovskite enabled a synergistic effect of efficient charge extraction and defect passivation.[127] In our most recent study on Sn–Pb narrow-bandgap perovskite photovoltaic devices (Fig. 9(c)), we innovatively proposed a grain boundary dipole modulation strategy, which reconfigures the grain boundaries from "recombination centers" into "charge separation channels." This strategy overcomes the conventional single-function paradigm of additive-based defect passivation, realizing a benign role of grain boundaries and demonstrating our team's capability in multiscale energy level regulation.[128]

6.2. Our work toward device stability

Although the photovoltaic efficiency of organic–inorganic hybrid perovskite solar cells (PSCs) has made tremendous progress, the intrinsic instability of volatile organic cations in hybrid perovskites under external stimuli seriously restricts their commercial application. One alternative to address this issue is the use of cesium (Cs) to fabricate all-inorganic perovskites $CsPbX_3$ (X = I, Br), which present superior thermal stability and optoelectronic properties. However, due to the rapid and difficult-to-control crystallization of inorganic perovskites, the resulting crystals usually exhibit suboptimal quality and morphology with numerous surface defects, leading to poor stability of thin films and devices. Employing self-polymerizing acrylate monomers (DPHA) during thermal treatment forms a network polymer that simultaneously passivates undercoordinated Pb^{2+} defects and serves as a hydrophobic protective barrier. The DPHA-based device achieved a record-high fill factor of 85.05% and a PCE of 20.05% (Fig. 9(d)). Crucially, DPHA-based films exhibited significantly enhanced phase and ambient-air stability, attributed to improved hydrophobicity and reduced defect density.[129] By introducing a hydrolysable 3-iodopropyltrimethoxysilane (IPTMS) additive into the $CsPbI_3$

CPB Online In-Press

precursor, we found that IPTMS can undergo *in-situ* polymerization via hydrolysis to form a hydrophobic polysiloxane network at grain boundaries during annealing (Fig. 9(e)). This process slows crystallization, consumes moisture, and passivates defects via I–Pb interactions, achieving the highest PCE of 20.36% for inverted PSCs with enhanced moisture stability. Even under high-humidity fabrication (80% RH), it retained an efficiency of 19.50%, demonstrating a broad processing window.[130] These results collectively demonstrate that rational interfacial engineering and molecular additive design are effective strategies for simultaneously improving the efficiency and stability of inorganic PSCs.

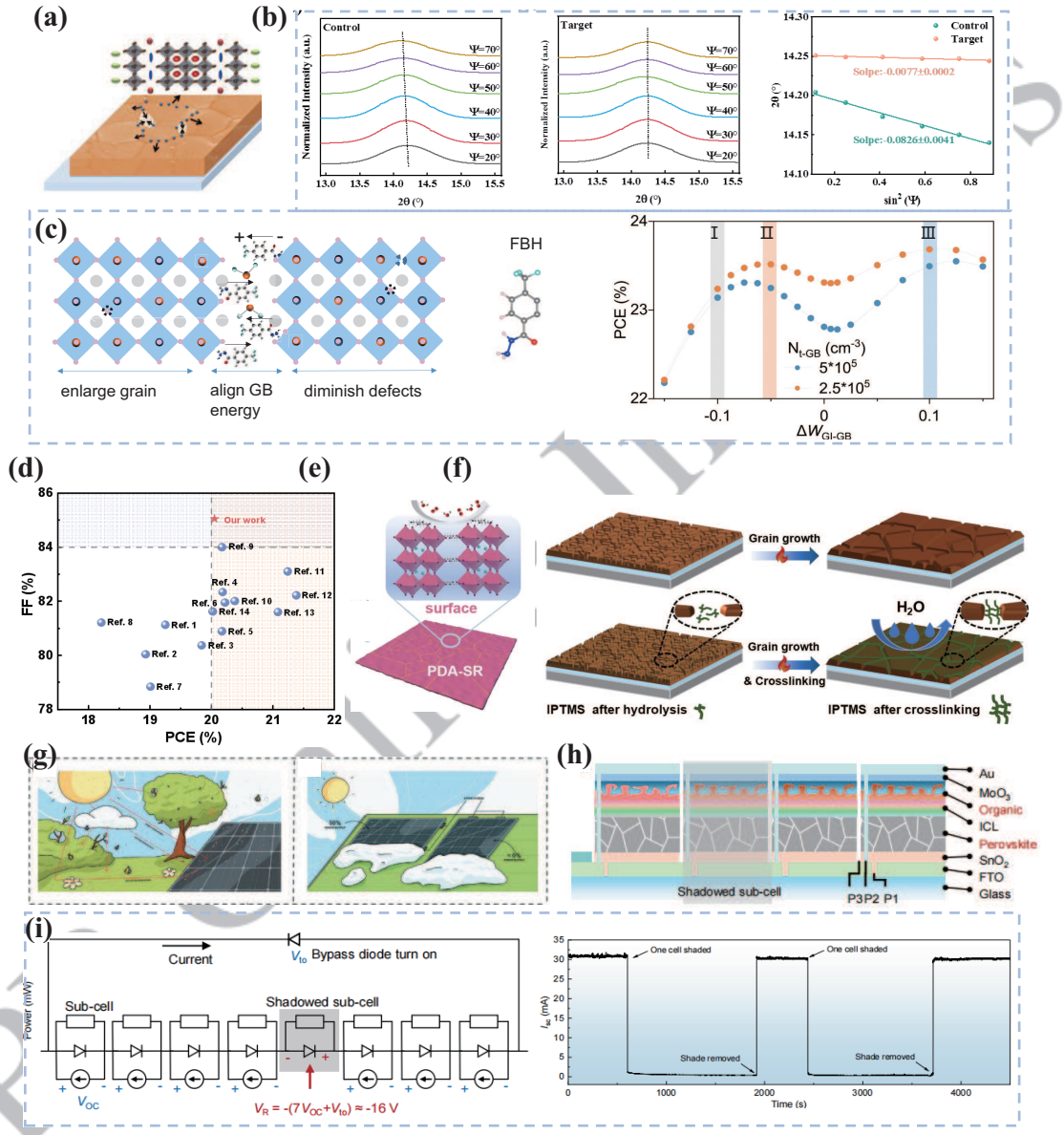


Fig. 9. (a) Schematic diagram of the mechanism of Zn ion doping.[122] (b) Grazing incidence x-ray diffraction (GIXRD) patterns of the control and target perovskite films. Macroscopic residual-strain distribution analysis by linear fitting for the control and target film.[123] (c) The scheme of total effects of FBH in perovskite film and numerical simulations of the device performance under different N_{t-GB} and ΔW_{GI-GB} in the perovskite film.[128] (d) PCE and FF distributions of this study and reported efficient inverted $CsPbI_3$ PSCs.[129] (e) Schematic diagram of $CsPbI_3$ perovskite grain growth without and with an IPTMS additive.[130] (f) Shadowing effect: solar panel partially shaded by vegetation, cloud, and snow from the sunlight.[131] (g) Schematic and equivalent circuit diagram of the module when one cell is under a shadow. (h) Current output of two minimodules connected in series when one cell was shaded and the shade was removed.[133]

Most present research on the stability of PSCs focuses on the effects of temperature, humidity, oxygen, and ultraviolet light, while stability under reverse bias has been rarely studied among the many factors. When large-area application of PSC panels occurs, the shading effect and local hot spots of PSC modules in real scenarios all indicate that the research on reverse bias stability of PSCs is urgently needed (Fig. 9(f)). We have reviewed the recent advances on the reverse bias stability issue, and the reverse bias behavior of PSCs is obtained, and the related mechanisms behind that have been proposed so far are reviewed and discussed. Furthermore, future directions are provided for further improving

the reverse bias stability of PSCs via increasing the reverse breakdown voltage (V_{RB}).[131,132] As shown in Fig. 9(g), we have significantly improved the reverse bias stability of PSCs and the shadow effect tolerance of their small module using the tandem concept. We firstly elucidate the mechanism that reverse tunnelling in organic solar cells (OSCs), fundamentally dominated by deep trap state within a bulk heterojunction, triggering reversible/irreversible breakdowns under reverse bias. Then, high-performance OSCs with superior irreversible breakdown voltage exceeding −35 V were demonstrated. Moreover, through strategically shielding perovskite by OSC with suppressed reverse tunnelling, n–i–p perovskite-organic tandem solar cells maintain over 90% of the initial efficiency when subjected to −40 V. These tandem devices retain 90% and 97% of the initial efficiency after stressing at −20 V for 12 h and −4.5 V for 2000 h, respectively, outperforming all existing thin-film solar technologies. The exceptional reverse-bias stability under shadowing conditions was further demonstrated in scalable perovskite-organic tandem solar cell minimodules (Fig. 9(h)).[133]

7. Summary and outlook

Perovskite photovoltaics have entered a stage in which single-junction efficiency on rigid glass substrates is no longer the only relevant metric, and scenario-driven deployment has become the central question shaping the field. In this review, we have organized recent progress on perovskite solar cells around three application scenarios where the technology offers properties that conventional silicon photovoltaics cannot easily match. These are flexible and wearable PSCs, IPV, and ST-PSCs. For each scenario, we have summarized the dominant performance metrics, the materials and interface strategies developed to meet them, and representative device demonstrations, while identifying three recurring bottlenecks, namely defect-state regulation, interface engineering, and operational stability, that currently constrain the transition from laboratory cells to commercial modules.

Despite this progress, most scenario-specific PSC demonstrations remain at the proof-of-concept stage. Champion single-junction efficiencies have approached 27%, indoor PCE under 1000 lux LED illumination has surpassed 40%, and AVT values above 60% have been demonstrated for semi-transparent devices, yet the gap between champion-cell metrics and module-level performance under realistic conditions remains considerable. To close this gap, we propose the following directions for future research.

Scenario-specific testing protocols Standardized conditions are needed beyond AM 1.5G testing, including agreed bending radii and cycle counts for F-PSCs, LED and fluorescent spectra with T80/T90 lifetimes under continuous low-flux illumination for indoor PSCs, and consistent definitions of AVT, CRI, and light utilization efficiency for semi-transparent PSCs. Without such protocols, scenario-relevant figures of merit cannot enter standard photovoltaic certification routes.

Coupled treatment of defects, interface, and stability bottlenecks Halide segregation under low-flux illumination, mechanical delamination under repeated bending, and parasitic absorption at transparent electrode interfaces all trace back to ionic mobility and weak chemical adhesion within the perovskite stack. Mitigation strategies such as Lewis-base passivation, self-assembled monolayer contacts, and atomic-layer-deposited moisture barriers should be screened for transferability across scenarios rather than redeveloped in isolation.

Substrate, interface, and electrode co-design Materials advances optimized for rigid, opaque cells often fail to transfer to flexible, indoor, or transparent platforms. Low-temperature processing rules out several high-efficiency transport layers, wide-bandgap absorbers suffer phase instability rarely encountered at 1.5 eV, and ITO-free transparent electrodes impose optical and mechanical constraints absent from standard architectures. These elements should be treated as a coupled design problem from the outset of materials screening.

Lead management, cost, and recyclability in parallel with efficiency Encapsulation must be matched to scenario stress, with sweat and abrasion considered for wearables, long-term weathering for BIPV, and user contact for indoor modules. Lead-sequestering layers, low-lead or lead-free absorbers, and closed-loop recycling for lead halides and transparent substrates should advance alongside efficiency rather than as downstream concerns.

Table 2. Technical requests upon three scenarios.

Application	Main metrics	Focus	Challenge
F-PSCs	High mechanical durability and specific power; stability of optoelectronic properties under deformation	Low-temperature fabrication process, flexible substrates and electrodes	Flexural stability, lead leakage
IPV	Low-light PCE and stability	Wide bandgap, low leakage current	Lack of testing standards, phase separation
ST-PSCs	Average visible light transmittance, light utilization efficiency, color rendering index	Selective absorption, transparent electrode	Large-area uniformity, packaging

Our group has focused on PSCs for 13 years and has developed special methods for efficiency improvement and stability enhancement. We will also focus on the commercial re-

CPB Online In Press

alization of PSCs related to their special properties. With coordinated progress along the directions above, perovskite photovoltaics will mature over the coming decade from scenario-specific demonstrations into commercially deployable systems, occupying roles in flexible electronics, indoor IoT, and building- or vehicle-integrated power generation that silicon cannot reach.

Acknowledgments

Project supported by the National Natural Science Foundation of China (Grant No. 62174094), Ningbo Youth Science and Technology Innovation Leading Talent Project (Grant No. 2023QL032), the Graduate Student Scientific Research and Innovation Project of Ningbo University (Grant No. IF2025010), and the K. C. Wong Magna Fund in Ningbo University, China.

References

[1] Chu S and Majumdar A 2012 *Nature* **488** 294
[2] Thampy S, Xu W and Hsu J W P 2021 *J. Phys. Chem. Lett.* **12** 8495
[3] Li Q, Liu Y, Guo S and Zhou H 2017 *Nano Today* **16** 46
[4] Cook T R, Dogutan D K, Reece S Y, Surendranath Y, Teets T S and Nocera D G 2010 *Chem. Rev.* **110** 6474
[5] Kojima A, Teshima K, Shirai Y and Miyasaka T 2009 *J. Am. Chem. Soc.* **131** 6050
[6] Lee M M, Teuscher J, Miyasaka T, Murakami T N and Snaith H J 2012 *Science* **338** 643
[7] Wang D, Li S and Ding Z 2026 *Nature* **654** 69
[8] Nazir G, Rehman A, Gautam J, Ikram M, Hussain S, Aftab S, Heo K, Lee S Y and Park S J 2025 *Adv. Powder Mater.* **4** 100304
[9] Shin S, Liu R, Yang Y, Lasalde-Ramírez J A, Kim G, Won C, Min J, Wang C, Fan K, Han H, *et al.* 2025 *Sci. Adv.* **11** eadw9024
[10] Egger D A, Bera A, Cahen D, Hodes G, Kirchartz T, Kronik L, Lovrincic R, Rappe A M, Reichman D R and Yaffe O 2018 *Adv. Mater.* **30** 1800691
[11] Feng J 2014 *APL Mater.* **2** 081801
[12] Eperon G E, Burlakov V M, Docampo P, Goriely A and Snaith H J 2014 *Adv. Funct. Mater.* **24** 151
[13] Liu T, Chen K, Hu Q, Zhu R and Gong Q 2016 *Adv. Energy Mater.* **6** 1600457
[14] Kim Y Y, Yang T Y and Suhonen 2020 *Nat. Commun.* **11** 5146
[15] Young J and Rondinelli J M 2016 *J. Phys. Chem. Lett.* **7** 918
[16] De Wolf S, Holovsky J, Moon S J, Löper P, Niesen B, Ledinsky M, Haug F J, Yum J H and Ballif C 2014 *J. Phys. Chem. Lett.* **5** 1035
[17] Noh J H, Im S H, Heo J H, Mandal T N and Seok S I 2013 *Nano Lett.* **13** 1764
[18] Guo Z, Jena A K and Miyasaka T 2023 *ACS Energy Lett.* **8** 90
[19] Lee D R, Kim M, Jeon S K, Hwang S, Lee C W and Lee J Y 2015 *Adv. Mater.* **27** 5861
[20] Jiang H, Feng J, Zhao H, Li G, Yin G, Han Y, Yan F, Liu Z and Liu S 2018 *Adv. Sci.* **5** 1801117
[21] Wu S, Li Z, Zhang J, Wu X, Deng X, Liu Y, Zhou J, Zhi C, Yu X, Choy W C H, *et al.* 2021 *Adv. Mater.* **33** 2105539
[22] Lai H, Luo J, Zwirner Y, Olthof S, Wieczorek A, Ye F, Jeangros Q, Yin X, Akhundova F, Ma T, *et al.* 2022 *Adv. Energy Mater.* **12** 2202438
[23] Sun Q, Duan S, Liu G, Meng X, Hu D, Deng J, Shen B, Kang B and Silva S R P 2023 *Adv. Energy Mater.* **13** 2301259
[24] Kokaba M R, Ahmed Y, Yeddu V, Zhang D, Moazzezi P, Kamraninejad V, Dayneko S, Reinecke S B, Amaro A, Villarejo B, *et al.* 2024 *Sol. RRL* **8** 2301013
[25] Wang C, Zhang C, Wang Q, Li H, Wu Y, Zhao Y, Chen S, Li L, Nie M, Song J, *et al.* 2025 *Adv. Sci.* **13** e09724
[26] Shen F, Zhao C, Li L, Xu J, Chen J, Wang X, Liu H, Zou P, Liu X, Fu Y, *et al.* 2026 *Adv. Funct. Mater.* **36** e75154
[27] Zhang X, Wu S, Zhang H, Jen A K Y, Zhan Y and Chu J 2024 *Nat. Photonics* **18** 1243
[28] Xu Z, Zhuang Q, Zhou Y, Lu S, Wang X, Cai W and Zang Z 2023 *Small Struct.* **4** 2200338
[29] Dissanayake P, Hoang M T, Senanayake S, Chiu W-H, Martens W, Qi D C, Klein M, Pandey A K, Yang Y and Wang H 2025 *Sol. Energy Mater. Sol. Cells* **293** 113826
[30] Castriotta L A, Uddin M A, Jiao H and Huang J 2025 *Adv. Mater.* **37** 2408036
[31] Dai X, Deng Y, Van Brackle C H, Chen S, Rudd P N, Xiao X, Lin Y, Chen B and Huang J 2020 *Adv. Energy Mater.* **10** 1903108
[32] Gao L, Chao L, Hou M, Liang J, Chen Y, Yu H D and Huang W 2019 *npj Flex. Electron.* **3** 4
[33] Chen L, Ingabire P B, Sun J, Xiong J, Cui C and Du P 2025 *Nano Energy* **142** 111197
[34] Chander S and Kaur I 2026 *Chem. Eng. J.* **530** 173368
[35] Sun L, Wang T, Wang Y, Li G, Deng Z, Sun S, Tan H, Wang X, Chen J, Peng L, *et al.* 2025 *Adv. Energy Mater.* **15** 2405581
[36] Xu W, Chen B, Zhang Z, Liu Y, Xian Y, Wang X, Shi Z, Gu H, Fei C, Li N, *et al.* 2024 *Nat. Photonics* **18** 379
[37] Truong M A, Funasaki T, Ueberricke L, Nojo W, Murdey R, Yamada T, Hu S, Akatsuka A, Sekiguchi N, Hira S, *et al.* 2023 *J. Am. Chem. Soc.* **145** 7528
[38] Wang X, Faizan M, Zhou K, Wang X, Fu Y and Zhang L 2024 *Chin. Phys. B* **33** 107303
[39] Pan Z, Yang J and Shen X 2024 *Chin. Phys. B* **33** 038501
[40] Han R, Weng P, Huangfu Y, Dong S, Zhang X, Shang C, Wang C, Zhou B, Qu D, Zhang Z, *et al.* 2026 *Adv. Mater.* **38** e72859
[41] Zhu P, Chen C, Dai J, Zhang Y, Mao R, Chen S, Huang J and Zhu J 2024 *Adv. Mater.* **36** 2307357
[42] Ma Y, Zhang M, Lin X, Cheng S, Wang L, Yang Y, Wu M, Tan H, Wu S, Fan J, *et al.* 2026 *Adv. Funct. Mater.* **36** e74890
[43] Li M, Gao H, Li L, Wang E, Liu Z, Cheong I T, Wu P, Zhang Y, Wang Y, Zheng X, *et al.* 2025 *Nat. Photonics* **19** 1255
[44] Liu J, Zheng D, Wang K, Li Z, Liu S, Peng L and Yang D 2024 *Joule* **8** 944
[45] Wang Y, Chang W, You W, Xue H, Zhou Y and Zhou J 2025 *Angew. Chem. Int. Ed.* **64** e202512376
[46] Saifi S, Xiao X, Cheng S, Guo H, Zhang J, Müller-Buschbaum P, Zhou G, Xu X and Cheng H M 2024 *Nat. Commun.* **15** 6546
[47] Kim U, Han M, Jang J, Shin J, Park M, Byeon J and Choi M 2023 *Adv. Energy Mater.* **13** 2203198
[48] Zhao J, Xu Z, Zhou Z, Xi S, Xia Y, Zhang Q, Huang L, Mei L, Jiang Y, Gao J, *et al.* 2021 *ACS Nano* **15** 10597
[49] Dong Z, Li W, Wang H, Jiang X, Liu H, Zhu L and Chen H 2021 *Sol. RRL* **5** 2100370
[50] Li C, Cong S, Tian Z, Song Y, Yu L, Lu C, Shao Y, Li J, Zou G, Rümmeli M H, *et al.* 2019 *Nano Energy* **60** 247
[51] Hailegnaw B, Demchyshyn S, Putz C, Lehner L E, Mayr F, Schiller D, Pruckner R, Cobet M, Ziss D, Krieger T M, *et al.* 2024 *Nat. Energy* **9** 677
[52] Liu T and Yang Z Y 2025 *SmartMat* **6** e70033
[53] Kumar J, Solangi N H, Neiber R R, Bai F, Charles V, Zhai P, Wang Z and Yang X 2026 *Nano-Micro Lett.* **18** 97
[54] Chakraborty A, Lucarelli G, Xu J, Skafi Z, Castro-Hermosa S, Kaveramma A B, Balakrishna R G and Brown T M 2024 *Nano Energy* **128** 109932
[55] Mathews I, Kantareddy S N, Buonassisi T and Peters I M 2019 *Joule* **3** 1415
[56] Grandhi G K, Koutsourakis G, Blakesley J C, De Rossi F, Brunetti F, Öz S, Sinicropi A, Parisi M L, Brown T M, Carnie M J, Hoye R L Z and Vivo P 2025 *Nat. Rev. Clean Technol.* **1** 132
[57] Pirc M, Ajdič Ž, Uršič D, Jošt M and Topič M 2024 *ACS Appl. Energy Mater.* **7** 565
[58] Ren Z, Ovčar J, Leung T L, He Y, Li Y, Li D, Qin X, Mo H, Yuan Z, Bing J, Bucknall M P, Grisanti L, Ali M U, Bai P, Zhu T, Syed A A, Lin J, Wang J, Khaleed A, Sun W, Li G, Li G, Ng A M C, Ho-Baillie A W Y, Lončarić I, Popović J and Djurišić A B 2025 *Matter* **8** 101937

CPB Online First Press

[59] Mathews I, Kantareddy S N R, Sun S, Layurova M, Thapa J, Correa-Baena J, Bhattacharyya R, Buonassisi T, Sarma S and Peters I M 2019 *Adv. Funct. Mater.* **29** 1904072
[60] Mathews I, Kelly G, King P J and Frizzell R 2014 *2014 IEEE 40th Photovoltaic Specialist Conference (PVSC)* (Denver, CO, USA: IEEE) pp. 0510–13
[61] Guillén C 2024 *Electronics* **13** 3378
[62] Ma Q, Ma M, Liu L, Yang P, He W, Zhang X, Zheng J, Zhang C, Liu C, Wu S, *et al.* 2023 *Device* **1** 100174
[63] Jin J, Zhu Z, Ming Y, Zhou Y, Shang J, Wang S, Cui X, Guo T, Zhang D, Tang G, *et al.* 2025 *Nat. Commun.* **16** 90
[64] Wu M, Kuo C, Jhuang L, Chen P, Lai Y and Chen F 2019 *Adv. Energy Mater.* **9** 1970143
[65] Burwell G, Zeiske S, Caprioglio P, Sandberg O J, Kay A M, Farrar M D, Kim Y R, Snaith H J, Meredith P and Armin A 2024 *Sol. RRL* **8** 2400180
[66] Albishi M S, Alabdulkarem F I, Perrakis G, Alhuwaymel T F, Sabeeh A H, Alharbi A S, Alshamrani N R, Khawaji I H, Tzoganakis N, Aljomah M M, *et al.* 2026 *Mater. Adv.* **7** 4160
[67] Ma Q, Wang Y, Liu L, Yang P, He W, Zhang X, Zheng J, Ma M, Wan M, Yang Y, *et al.* 2024 *Energy Environ. Sci.* **17** 1637
[68] Zhang C, Liu C, Gao Y, Zhu S, Chen F, Huang B, Xie Y, Liu Y, Ma M, Wang Z, *et al.* 2022 *Adv. Sci.* **9** 2204138
[69] Orwat B, Shi Z, Ma C, Jankowska K, Nawrocik J, Singh A, Zheng Y, Tu W, Ling Z, Dąbczyński P, Rogala M, Krukowski P, Kowalczyk P J, Data P, Łuszczyńska B, Kownacki I and Chen C 2025 *Small* **21** 2411623
[70] Cheng R, Chung C C, Zhang H, Liu F, Wang W T, Zhou Z, Wang S, Djurišić A B and Feng S P 2019 *Adv. Energy Mater.* **9** 1970146
[71] Han Z, Wang Z, Xia Z, Zhang X, Yang J, Liu Y, Zhai Y, Li T, Zhang S, Wang L, *et al.* 2025 *Nat. Commun.* **16** 11470
[72] Xu J, Zhu X, Dai J, Zhang M, Wei X, Lei T, Xie H, Pan Y, Cao J, Wu Z, *et al.* 2025 *Chem. Eng. J.* **510** 161624
[73] Ma Y, Luo C, Zhan C, Wang K, He J, Gao P, Bi Z, Ma Y and Zhao Q 2025 *Sci. Adv.* **11** eady5703
[74] Jagadamma L K and Wang S 2021 *Front. Chem.* **9** 632021
[75] Wang Y, Ahmad I, Leung T, Lin J, Chen W, Liu F, Ng A M C, Zhang Y and Djurišić A B 2022 *ACS Mater. Au* **2** 215
[76] Domanski K, Alharbi E A, Hagfeldt A, Grätzel M and Tress W 2018 *Nat. Energy* **3** 61
[77] Dou D, Sun H, Li C, Gan S and Li L 2024 *Adv. Funct. Mater.* **34** 2314398
[78] Liu W, Zhou T, Chu L and Li X 2026 *Chin. Phys. B* **35** 028801
[79] Panda D P, Issaoui R, Iqbal Z, Grandhi G K, Ur Rehman M O, Zu F, Alippi P, Rastgoo M, Zuo S, Luzzi E, *et al.* 2025 *ACS Energy Lett.* **10** 3789
[80] Kin L C, Liu Z, Astakhov O, Shcherbachenko S, Kungl H, Kirchartz T, Eichel R-A, Rau U and Merdzhanova T 2022 *Cell Rep. Phys. Sci.* **3** 101123
[81] Liu T, Almutairi M M S, Ma J, Stewart A, Xing Z, Liu M, Hou B and Cho Y 2025 *Nano-Micro Lett.* **17** 49
[82] Ghosh A 2020 *J. Cleaner Prod.* **276** 123343
[83] Zhao Y, Zhu Y, Cheng H W, Zheng R, Meng D and Yang Y 2021 *Mater. Today Energy* **22** 100852
[84] Pulli E, Rozzi E and Bella F 2020 *Energy Convers. Manage.* **219** 112982
[85] Goje A A, Ludin N A, Sepeai S, Su'ait M S, Syafiq U and Chelvanathan P 2025 *Sol. Energy* **302** 113964
[86] Traverse C J, Pandey R, Barr M C and Lunt R R 2017 *Nat. Energy* **2** 849
[87] Pompilio M, Ierides I and Cacialli F 2022 *Molecules* **28** 180
[88] Xu C, Chen Y, Zhao Z, Yang B, Suo J, Ba K, Tarasov A, Wu Y, Lian X, Luo M, *et al.* 2025 *Energy Environ. Sci.* **18** 2095
[89] Mescher J, Kettlitz S W, Christ N, Klein M F G, Puetz A, Mertens A, Colsmann A and Lemmer U 2014 *Org. Electron.* **15** 1476
[90] Grifoni F, Bonomo M, Naim W, Barbero N, Alnasser T, Dzeba I, Giordano M, Tsaturyan A, Urbani M, Torres T, *et al.* 2021 *Adv. Energy Mater.* **11** 2101598
[91] Annabi Milani E, Piralaee M, Raeyani D and Asgari A 2024 *Sol. Energy Mater. Sol. Cells* **276** 113066
[92] Liu D, Sun Y, Wilson R and Wu Y 2020 *Renew. Energy* **145** 1399
[93] McCamy C S 1992 *Color Res. Appl.* **17** 142
[94] Chen Z, Yu X, Wang C, Khanh T Q and Liu Q 2025 *Build. Environ.* **269** 112436
[95] Jung J W, Chueh C C and Jen A K Y 2015 *Adv. Energy Mater.* **5** 1500486
[96] Kumar P, You S and Vomiero A 2023 *Adv. Energy Mater.* **13** 2301555
[97] Giannouli M 2021 *Int. J. Photoenergy* **2021** 6692858
[98] Manser J S, Christians J A and Kamat P V 2016 *Chem. Rev.* **116** 12956
[99] Kwon H C and Moon J 2018 *Curr. Opin. Electrochem.* **11** 114
[100] Wang H, Xu W, Wei Q, Peng S, Shang Y, Jiang X, Yu D, Wang K, Pu R, Zhao C, *et al.* 2023 *Light: Sci. Appl.* **12** 62
[101] Shao Y, Chen Q, Zheng G, Wei L, Chen B, Yao D, Tian N, Wang J, Mo S, Zhou B, *et al.* 2025 *ACS Appl. Mater. Interfaces* **17** 29583
[102] Wang Z, Zhu X, Zuo S, Chen M, Zhang C, Wang C, Ren X, Yang Z, Liu Z, Xu X, *et al.* 2020 *Adv. Funct. Mater.* **30** 1908298
[103] Zhou Y P, Ma X Y, Yang P X and He Y L 2023 *Mater. Today Chem.* **30** 101520
[104] Kulkarni S A, Baikie T, Boix P P, Yantara N, Mathews N and Mhaisalkar S 2014 *J. Mater. Chem. A* **2** 9221
[105] Yu J C, Li B, Dunn C J, Yan J, Diroll B T, Chesman A S R and Jasieniak J J 2022 *Adv. Sci.* **9** 2201487
[106] Mohamad Noh M F, Arzaee N A, Sadikin S N, Idris M I, Chau C F, Yap B K, Huang J, Ishikawa R and Mahmood Zuhdi A W 2026 *Nano-Micro Lett.* **18** 317
[107] Zhang R, Ma B, Cui Y, Tan C, Chen B, Li Y, Shi J, Wu H, Luo Y, Li D, *et al.* 2025 *Mater. Futures* **4** 045103
[108] Wang J, Wang L, Meng K, Liu P, Lu Y, Li J, Huang X, Yip H L and Li G 2026 *Adv. Funct. Mater.* **36** e75317
[109] Ghosh T, Mane P, Chakraborty B, Sahoo P K and Pradhan D 2023 *ACS Appl. Mater. Interfaces* **15** 17994
[110] Yan N, Yang F, Cao Y, Zhang J, Que M, Li B, Tang Y, Liu S and Feng J 2025 *Chem. Eng. J.* **522** 167416
[111] Tanty S, Noh Y I and Choi K J 2026 *Chem. Eng. J.* **534** 175135
[112] Matteocci F, Rossi D, Castriotta L A, Ory D, Mejaouri S, der Maur M A, Sauvage F, Cacovich S and Di Carlo A 2022 *Nano Energy* **101** 107560
[113] Mei J and Yan F 2025 *Adv. Mater.* **37** 2418622
[114] Chen J, Pan J, Duan B, Hou P, Zhang Y, Zhu Y, Lv T, Hu M, Zhao J, Xiao S, *et al.* 2026 *Adv. Energy Mater.* **16** e06610
[115] Jin J, Zhang J, Zhang J, Zou S, Xin Y, Du B, Yan X and Huang J 2025 *Adv. Energy Mater.* **15** e01994
[116] Yoon S, Ryu J, Cho S, Kim H D, Lim J, Cho J S, Park J and Kang D W 2025 *Small* **21** 2501876
[117] Datt R, Alsayyed H, Dhall S, Gupta S, Bishnoi S, Gupta R, Arya S, Watson T and Tsoi W C 2025 *Discov. Appl. Sci.* **7** 1348
[118] Huang Y, Liu X, Kalogirou S A, Duan X, Mi W, Wang J, Jiao K and Shen C 2026 *Renew. Sustain. Energy Rev.* **234** 116884
[119] Paliwal A, Romero M, van den Hengel L, Rodkey N, Zanoni K P S, Lozano G, Roldán-Carmona C, Sessolo M, Míguez H and Bolink H J 2025 *Adv. Mater.* **38** e12861
[120] Yoon S, Lee I H, Han J, Bahadur J, Lee S, Lee S, Kim D S, Mikladal B, Kauppinen E I, Kang D W and Jeon I 2024 *EcoMat* **6** e12440
[121] Zheng J, Zhu W, Xiong J, Wang Q, Xuan R, Sun X, Gan X, Liu X, Huang L, Zhu Y, *et al.* 2025 *ACS Appl. Mater. Interfaces* **17** 1110
[122] Sun H, Zhang J, Gan X, Yu L, Yuan H, Shang M, Lu C, Hou D, Hu Z, Zhu Y, *et al.* 2019 *Adv. Energy Mater.* **9** 1900896
[123] Xiong J, Wang Q, Xing Y, Gan X, Zhu W, Xuan R, Huang L, Liu X, Zhu Y and Zhang J 2024 *Small* **20** 2400934
[124] Zhang Z, Fang Z, Guo T, Zhao R, Deng Z, Zhang J, Shang M, Liu X, Liu J, Huang L, *et al.* 2022 *Chem. Eng. J.* **432** 134311
[125] Zhang J, Shang M, Wang P, Huang X, Xu J, Hu Z, Zhu Y and Han L 2016 *ACS Energy Lett.* **1** 535
[126] Zhang J, Chen R, Wu Y, Shang M, Zeng Z, Zhang Y, Zhu Y and Han L 2018 *Adv. Energy Mater.* **8** 1701981
[127] Guo T, Wang H, Han W, Zhang J, Wang C, Ma T, Zhang Z, Deng Z, Chen D, Xu W, *et al.* 2022 *Nano Energy* **98** 107298
[128] Xiong J, Ma T, Shi L, Zhang J, Xu Y, Wang Q, Zhu W, Xuan R, Yang Z, Wang C, *et al.* 2026 *Adv. Mater.* **38** e72755
[129] Liu Z, Huang X, Zhao Y, Wang J, Liu J, Zhou C, Wang H, Cui T and Liu X 2025 *J. Energy Chem.* **108** 381
[130] Liu J, Liu X, Wang J, Liu Z, Zhou C, Zeng H, Qiao H, Zhang J, Huang L, Chen N, *et al.* 2025 *J. Phys. Chem. Lett.* **16** 8632
[131] Wang C, Huang L, Zhou Y, Guo Y, Liang K, Wang T, Liu X, Zhang J, Hu Z and Zhu Y 2023 *Adv. Energy Mater.* **13** 2203596
[132] Kang S, Zhang J, Liang H, Huang J, Ren Z, He T, Liu X, Zhang J, Zhu Y, Liu K, *et al.* 2026 *Adv. Energy Mater.* 16 e06005
[133] Huang J, Han Y, Ren Z, *et al.* 2026 *Nat. Mater.* **25** 1419

CPB Online First Press